JOURNAL OF GEOPHYSICAL RESEARCH, VOL. 104, NO. D14, PAGES 16,807–16,826, JULY 27, 1999

Radiative forcing by volcanic aerosols from 1850 to 1994

Natalia G. Andronova, Eugene V. Rozanov, Fanglin Yang, and
Michael E. Schlesinger
Department of Atmospheric Sciences, University of Illinois at Urbana-Champaign, Urbana

Georgiy L. Stenchikov
Department of Environmental Sciences, Rutgers University, New Brunswick, New Jersey

Abstract. We use our detailed radiative transfer model and the latitude-altitude distributions of zonal mean optical properties for the Pinatubo aerosol to calculate the time evolution of its instantaneous radiative forcing. We represent the zonal mean of this radiative forcing in terms of the zonal mean optical depth of the Pinatubo aerosol, together with the solar insolation, effective emitting temperature, daylight fraction of a day, and the planetary albedo in the absence of the aerosol. We use this representation, together with the volcano optical depths compiled by *Sato et al.* [1993], to calculate the instantaneous and adjusted radiative forcing by volcanic aerosols from 1850 to 1994.

1. Introduction

The 1995 Intergovernmental Panel on Climate Change (IPCC) report [*Schimel et al.,* 1996] states that "the decadal mean radiative forcing due to volcanic aerosols in the stratosphere may have varied by as much as 1.5 W/m^2 since 1850; hence such a variation can be large compared to the decadal-scale variation in any other known forcing." It has been hypothesized [e.g., *Pollack et al.,* 1976] that volcanoes have contributed to the increase in global-mean surface-air temperature that has been observed from the middle of the 19th century to the present. This hypothesis states that although the net radiative forcing of a volcano is negative, and thus major volcanoes result in a cooling of the global-mean surface-air temperature for 1 to 2 years, the decrease in the number of major volcanoes from the 19th to the 20th centuries resulted in a relative warming of the climate. However, it has been difficult to test the volcano-climate hypothesis quantitatively because of the large uncertainty about the radiative forcing by volcanoes, the change in net radiation ΔN, either at the top of the atmosphere (TOA) or at the tropopause.

This uncertainty in the ΔN due to volcanoes exists because of our lack of knowledge about the altitude at which volcanic gases have been injected into the stratosphere, the composition and dispersion of the volcanic aerosol created therefrom by gas-to-particle conversion, and the radiative properties of these volcanic aerosols. While this ignorance about past volcanoes renders impossible the calculation of their radiative forcing by comprehensive radiative transfer models (RTMs), such RTM calculations for putative volcanic aerosols have indicated that their radiative forcing at the top of the atmosphere and at the tropopause can be determined from their optical depth τ alone; that is, $\Delta N = \beta\tau$, where β is a regression coefficient. This is useful because the latitude-time distribution of τ following the major volcanic eruptions from 1850 to 1994 has been compiled by *Sato et al.* [1993] (hereinafter referred to as SA93). In Table 1 we present four model estimates of β, two for the net radiative forcing at the top of the atmosphere and two for the net radiative forcing at the tropopause. Also, in Table 1 we present the observations by the NOAA-11 and ERBE satellites of the net radiative forcing from 40°S to 40°N by the most recent major volcano, Pinatubo. Table 1 shows that the estimate of β for the net radiative forcing at the top of the atmosphere ranges from –7.1 to –19.2 W/m^2.

One can reduce the uncertainty in the estimate of the volcanic radiative forcing by using a comprehensive RTM to calculate the radiative forcing for the Pinatubo volcanic aerosol. This volcanic aerosol was observed more intensively and completely by satellite-based and ground-based instruments than any other volcanic aerosol. We do so herein using our RTM and then represent the radiative forcing for the Pinatubo volcanic aerosol in terms of τ and other quantities. Lastly, we use this representation together with the compilation of τ by SA93 to calculate the radiative forcing by volcanic aerosols from 1850 to 1994. We note that by using our RTM, we calculate the instantaneous radiative forcing. As mentioned by *Lacis et al.* [1992] and supported by IPCC [*Harvey et al.,* 1997], to estimate the climatic effect of volcanic aerosols, one should use the "adjusted" radiative forcing at the tropopause, i.e., the radiative forcing after the stratosphere is allowed to adjust radiatively to the perturbation.

The most recent calculation of the instantaneous radiative forcing by the Pinatubo volcanic aerosol was performed by *Stenchikov et al.* [1998] (hereinafter referred to as ST98). ST98 derived the monthly zonal-mean aerosol optical properties from the observed data and used these optical properties together with the ECHAM4 atmospheric General Circulation Model (GCM) to calculate the radiative forcing by the Pinatubo aerosol. Unfortunately, a disadvantage of the ECHAM4 GCM is its relatively coarse spectral and vertical resolutions. In particular, the ECHAM4 RTM has two spectral intervals in the solar (one in the visible (0.25 ~ 0.68 μm) and one interval in the near-IR (0.68 ~ 4 μm)) and seven intervals in the longwave (3.56 μm to 250 μm), and the ECHAM4 GCM has 19 vertical levels, with the top layer extending from p = 0 hPa to 20 hPa.

Accordingly, this study has three main goals: (1) to calculate the instantaneous radiative forcing by the Pinatubo aerosol using the RTM of the UIUC (University of Illinois at Urbana-Champaign) GCM, which has higher spectral and vertical resolutions than the ECHAM4 GCM used by ST98; (2) to parameterize the individual instantaneous and adjusted solar and longwave radiative forcing by the Pinatubo aerosol in terms of optical depth

Paper number 1999JD900165
0148-0227/99/1999JD900165$09.00

Table 1. Theoretical and Observational Estimation of Net, Solar, and Longwave Radiative Forcings Due to Volcanic Aerosol

Study	Net Radiative Forcing ΔN, W/m^2	Solar Radiative Forcing ΔS, W/m^2	Longwave Radiative Forcing $-\Delta R$, W/m^2
	Top of the Atmosphere (TOA)		
Stowe et al. [1992] [a]	-19.2τ	-33.1τ	13.8τ
Chou et al. [1984] [a,c]	-13.0τ	-22.3τ	9.3τ
Minnis et al. [1993] [b]	$-(11.5\pm4.4)\tau - 0.5$	$-(17.1\pm5.6)\tau - 0.7$	$-(7.9\pm5.1)\tau - 1.9$
	Tropopause (TR)		
Lacis et al. [1992] [a]	-30.0τ [(d)]		
Hansen et al. [1997]	instantaneous, -28.4τ adjusted, -26.8τ		

[a] Theoretical calculation.

[b] Satellite observations.

[c] From Table 1, case A.

[d] It is not clear whether this radiative forcing is instantaneous or adjusted.

and other quantities; and (3) to calculate the historical radiative forcing by volcanoes.

In section 2 we present the new calculation of the instantaneous radiative forcing by the Pinatubo aerosol. The search for quantities in addition to optical depth that should be included in the parameterization of the volcano radiative forcing is described in section 3 on the basis of calculations with a single-column (one-dimensional ("1-D")) RTM. In section 4 the approximation for the instantaneous and adjusted solar and longwave radiative forcing in terms of the aerosol optical depth, solar insolation, daylight fraction of a day, planetary albedo, and effective emitting temperature are obtained on the basis of calculations with a multiple-column ("3-D") RTM. These expressions are used in section 5, together with the volcano aerosol optical depths compiled by SA93, to calculate the radiative forcing by volcanic aerosols from 1850 to 1994. Our conclusions are presented in section 6.

2. Calculation of Radiative forcing by Pinatubo aerosol

In this section we use the RTM of the UIUC 24-layer stratosphere/troposphere general circulation model (ST/GCM) to calculate the time-latitude distribution of zonal-mean radiative forcing by the Pinatubo aerosol from June 1991 to May 1993. Below, we describe the radiative transfer model (section 2.1), the calculated optical properties of the Pinatubo aerosol (section 2.2), and the calculated radiative forcing by the Pinatubo aerosol (section 2.3).

2.1. Radiative Transfer Model

The radiative transfer model (RTM) has 24 layers from the Earth's surface to 1 hPa (*F. Yang et al.*, manuscript in preparation, 1999). The calculation of terrestrial (longwave) radiation in the RTM is based mainly on the parameterization of *Chou and Suarez* [1994] and includes the absorption and emission of longwave radiation by water vapor, carbon dioxide, ozone, clouds, aerosol, and the trace gases N_2O, CH_4, CFC-11, CFC-12, and HCFC-22. The longwave spectrum from 3000 cm^{-1} to zero is divided into nine broadbands. The effect of clouds on longwave radiation is included by introducing a mean flux transmittance that is the product of the gaseous transmittance and a cloud-related coefficient. This coefficient conveys information about cloudiness, cloud optical thickness, and cloud overlap. Clouds are grouped into three categories: high clouds above the 16th sigma layer of the model (~400 hPa), middle clouds between the 16th (~400 hPa) and the 19th layer (~700 hPa), and low clouds below the 19th layer. Clouds within each category are assumed to be maximally overlapped, and clouds between different categories are assumed to be randomly overlapped.

The calculation of solar radiation in the RTM is based mainly on the parameterization of *Chou* [1990, 1992] and *Chou and Lee* [1996]. The RTM has eight bands in the ultraviolet and visible spectral regions (0.175–0.7 μm) and three bands in the near-infrared and thermal-infrared regions (0.7–10.0 μm). The RTM calculates the absorption of solar radiation by water vapor, ozone, carbon dioxide, oxygen, clouds and aerosols, and the scattering by clouds, aerosols, and molecules (Rayleigh scattering), as well as reflection from the surface. Shortwave radiative properties of liquid-water clouds [*Slingo,* 1989] depend on the liquid-water path and the equivalent radius of the drop size distribution (r_e), the latter of which is determined by the in-cloud liquid-water content and cloud droplet number concentration (CDNC). The CDNC is empirically related to the aerosol mass concentration [*Boucher and Lohmann,* 1995]. In this study we fixed $r_e = 10$ μm so that there would be no indirect (cloud) radiative forcing by the volcanic aerosols, which would result if r_e were variable. Absorption of longwave radiation and absorption and scattering of shortwave radiation by the tropospheric natural sulfate aerosol [*Langner and Rodhe,* 1991] are included. Solar radiative properties of ice clouds are functions of ice-water path and ice crystal effective size, assumed to be 75 μm. Ice-and liquid-water clouds are allowed to coexist in the same GCM grid cell. For mixed-phase clouds the optical depth is the summation of the water-cloud and ice-cloud optical depths, the single-scattering albedo is optical-depth weighted, and the asymmetry factor is optical-depth and single-scattering albedo weighted. The delta-Eddington method is used to calculate transmittance and reflectance of each layer [*King and Harshvardhan,* 1986], and then the two-stream adding method of *Chou* [1992] is applied to compute the upward and downward fluxes in both the clear and the cloudy atmosphere.

The UIUC RTM described above has a finer spectral resolution than the ECHAM4 RTM used in ST98 to calculate instantaneous Pinatubo aerosol forcing. Accordingly, the Pinatubo aerosol radiative forcing calculated here using the UIUC RTM is likely more accurate than that calculated by ST98 using the ECHAM4 RTM.

2.2. Radiative Properties of Pinatubo Aerosol

To calculate the radiative forcing by the Pinatubo aerosol using the RTM of the UIUC 24-layer ST/GCM requires the time and spatially varying broadband-averaged aerosol extinction, single-scattering albedo, and asymmetry factor. We use the same approach and model package that ST98 used to derive the monthly zonal-mean aerosol optical properties. The only differences here from ST98 are (1) all vertical interpolations are performed such that the total optical depth for 1.02 μm was conserved, and (2) for consistency, the derivation is performed for the spatial grid and spectral bands of the UIUC 24-layer ST/GCM. Both of these differences improve the calculation of the optical properties of the volcanic aerosol. The first difference is important because it correctly defines the total number of aerosol particles in the column in the spectral band where the most representative observational data exist, and the second difference improves the vertical and spectral representation of the Pinatubo aerosol cloud. The atmospheric conditions that are required to derive the aerosol optical properties, such as the geopotential heights of isobaric surfaces, were obtained from the climatology simulated by the UIUC 24-layer ST/GCM (*F. Yang et al.*, manuscript in preparation, 1999).

Because of the differences between the calculations of the aerosol optical properties performed here and by ST98, we compare the optical depth calculated for the two models with each other and with observations. Figure 1 presents the monthly mean column-integrated optical depths at $\lambda = 0.55$ μm and $\lambda = 1.02$ μm for the period June 1991 to May 1993 calculated for the UIUC 24-layer ST/GCM (Figures 1a and 1e) and for the ECHAM4 GCM (ST98) (Figures 1b and 1f), and as observed by SAGE II at $\lambda = 0.525$ μm and $\lambda = 1.02$ μm (Figures 1c and 1g) and AVHRR at $\lambda = 0.55$ μm (Figure 1d).

The optical depth at $\lambda = 0.55$ μm calculated for the UIUC ST/GCM (Figure 1a) has a similar latitude-time distribution as the optical depth calculated for the ECHAM4 GCM (ST98) (Figure 1b) but is generally larger, especially in the middle and high latitudes where our optical depth reaches 0.15 to 0.25, while the ST98 was only about 0.1. Also, the calculations for the UIUC ST/GCM reveal a secondary optical-depth maximum in the high latitudes of both hemispheres, which is absent in ST98. Calculation of the column-integrated optical depth for $\lambda = 0.55$ μm for the UIUC ST/GCM agrees better with the Advanced Very High Resolution Radiometer (AVHRR) observation (Figure 1d) than with the optical depth of ST98, even though both calculated optical depths are smaller than observed by AVHRR. As mentioned by *Long and Stowe* [1994], the AVHRR data may overestimate the optical depth because of the deficiency of the retrieval algorithm. The discrepancy between the SAGE II (Figure 1c) and the AVHRR data defines the level of observational uncertainty.

Comparison of Figures 1e–1g shows that as expected, the calculations of the column-integrated optical depth at $\lambda = 1.02$ μm for the UIUC ST/GCM agree exactly with the SAGE II observations, while the ST98 optical depths underestimate it, especially in the middle and high latitudes of both hemispheres.

In general, we explain the larger optical depths for both spectral intervals ($\lambda = 0.55$ μm and $\lambda = 1.02$ μm) obtained here for the UIUC ST/GCM than by ST98 for the ECHAM4 GCM as mostly due to our constraint on the calculation here of the optical depth at $\lambda = 1.02$ μm.

Figure 1h shows our calculation of the time-altitude distribution of aerosol extinction (1/m) at the equator for $\lambda = 0.55$ μm. It can be seen that a part of the aerosol cloud is located above 10 hPa. This high-altitude part of the aerosol cloud is better resolved by the UIUC ST/GCM than by the ECHAM4 GCM. This is an advantage of the UIUC ST/GCM. Overall, the UIUC ST/GCM gives an improved representation of the optical properties of the Pinatubo aerosol.

2.3. Instantaneous Radiative Forcing by Pinatubo Aerosol

Henceforth, we shall refer to the RTM of the UIUC ST/GCM as the 3-D RTM to distinguish it from the single-column version used in section 3, which we shall refer to as the 1-D RTM.

We define the net radiative flux as $N = S - R$, where S is the net incoming solar flux, defined as positive downward, and R is the outgoing terrestrial flux, defined as positive upward. The radiative forcing by the Pinatubo aerosol was calculated hourly by the 3-D RTM as $\Delta N = \Delta S - \Delta R$, where Δ is the difference between the radiative fluxes calculated by the 3-D RTM with and without the aerosol. The three-dimensional distributions of temperature, water vapor, cloud cover, and cloud-water/ice mixing ratio used for this calculation were taken from the present-day (control) simulation by the 24-layer ST/GCM for prescribed climatological sea surface temperatures (*F. Yang et al.*, manuscript in preparation, 1999). The RTM calculation covered the time period from June 1991 to May 1993. For each latitude, vertical layer and spectral band of the 3-D RTM, monthly mean values of the zonal-mean extinction coefficient, single-scattering albedo, and asymmetry factor for the Pinatubo volcano (section 2.2) were prescribed at each of the RTM longitudes. These monthly mean optical properties were kept unchanged during the hourly radiative forcing calculation within each month. The final product, the monthly zonal-mean radiative forcing, was obtained by averaging the hourly 3-D radiative forcing temporally and longitudinally for each month.

Figures 2a and 2b respectively present the net radiative forcing, ΔN, at the top of the model (1 hPa) and at the tropopause (≈ 200 hPa) from June 1991 to May 1993. These figures show that the net radiative forcing is negative almost everywhere and is larger in magnitude at the tropopause than at the top of the model. The maximum negative net radiative forcing at both levels is located between 30°S and 30°N during more than half a year after the Pinatubo eruption. These results agree in general with the ST98 calculations. However, the maximum negative forcing we obtained at both levels for the first year after the Pinatubo eruption is larger than that of ST98. Also, the secondary maxima in the negative net radiative forcing in high latitudes of both hemispheres are larger in our calculations than in the calculations of ST98. The probable reasons for these differences are as follows: (1) the aerosol optical depth used in the UIUC calculations is larger than that in the ECHAM4 calculations; (2) the ECHAM4 GCM has a lower vertical resolution in the stratosphere than the UIUC ST/GCM and thus does not properly represent the aerosol optical properties above 10 hPa; (3) the ECHAM4 GCM has a lower spectral resolution and covers narrower spectral ranges for both solar and longwave radiation than the UIUC ST/GCM; and (4) the different geographical distributions of clouds, planetary albedo, and temperature simulated by the two GCMs may have influenced the radiative-forcing calculation. There are other factors that may have led to the differences in the radiative forcing calculated by the two models, for example, the time step for computing the solar radiation (1 hour for the UIUC 24-layer ST/GCM and 2 hours for the ECHAM4 GCM) as well as differences in the radiative transfer algorithms themselves. It would be very valuable to perform a model intercomparison study for the radiative forcing of the Pinatubo aerosol, similar to that performed for hypothetical aerosols by *Boucher et al.* [1998] for tro-

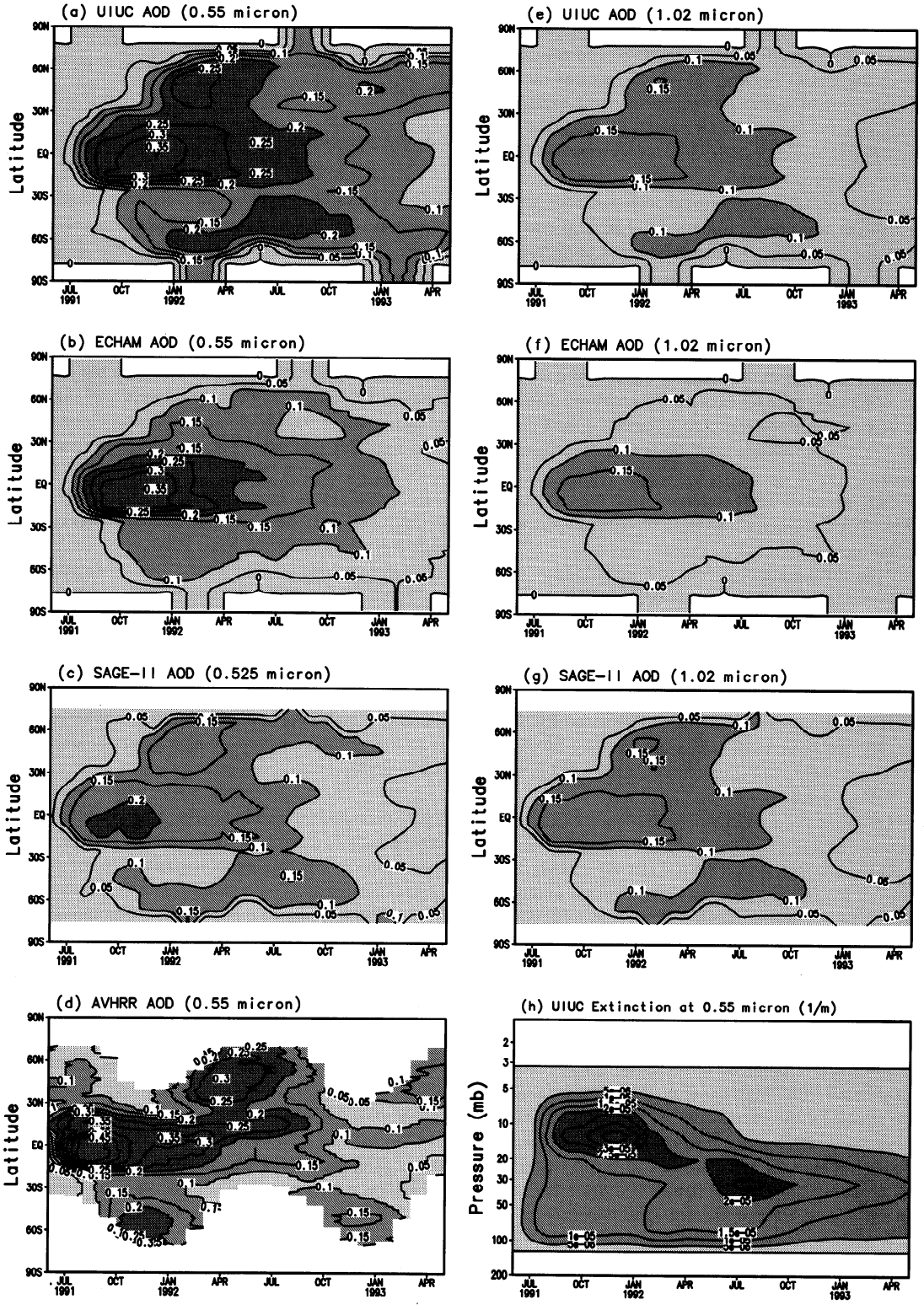

Figure 1. Time-latitude distributions of zonal-mean column-integrated optical depth: (a) calculated at $\lambda = 0.55$ μm for the RTM of the UIUC 24-layer ST/GCM; (b) calculated at $\lambda = 0.55$ μm by ST98 for the 19-layer ECHAM4 GCM; (c) observed at $\lambda = 0.525$ μm by SAGE II; (d) observed at $\lambda = 0.55$ μm by AVHRR; (e) calculated at $\lambda = 1.02$ μm for the RTM of the UIUC 24-layer ST/GCM; (f) calculated at $\lambda = 1.02$ μm by ST98 for the 19-layer ECHAM4 GCM; and (g) observed at $\lambda = 1.02$ μm by SAGE II. Figure 1h shows the time-altitude distribution of aerosol extinction at the equator calculated at $\lambda = 0.55$ μm for the RTM of the UIUC 24-layer ST/GCM.

pospheric sulfate aerosol, but such an intercomparison is beyond the scope of this paper.

The solar radiative forcings (0.175 – 10 μm), ΔS, at TOA and the tropopause are presented in Figures 2c and 2d. Comparison of these figures shows that the solar radiative forcing at both levels is negative and similar in shape and magnitude. The main feature of the solar radiative forcing is the presence of five areas of maximum negative forcing. The first negative forcing maxi-

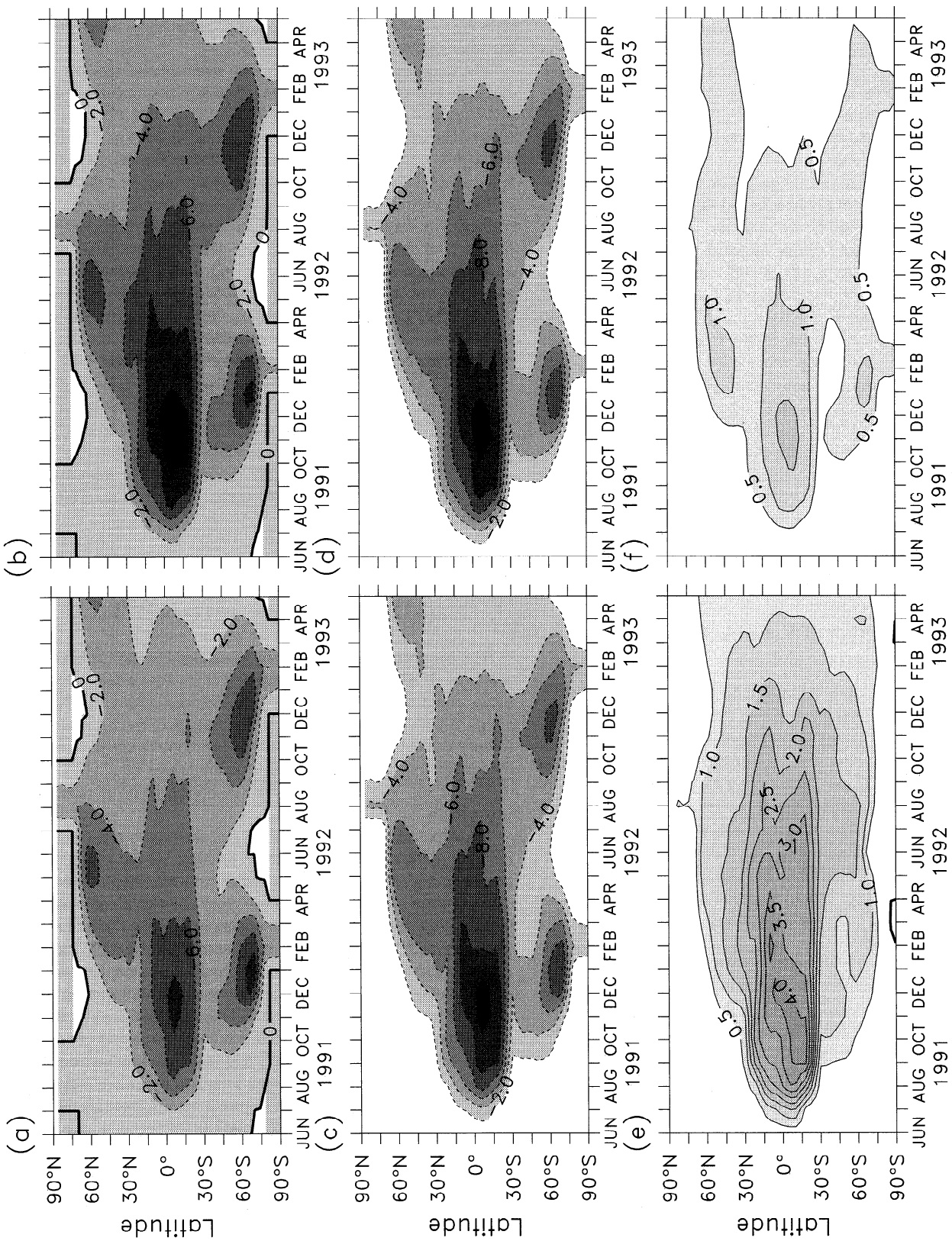

Figure 2. Latitude-time distributions at the top of the model (1 hPa, Figures 2a, 2c, and 2e) and at the tropopause (Figures 2b, 2d, and 2f) of the zonal-mean net radiative forcing, ΔN (Figures 2a and 2b), the solar radiative forcing ΔS (Figures 2c and 2d), and the longwave radiative forcing, $-\Delta R$ (Figures 2e and 2f), from June 1991 to May 1993.

mum is located in the tropics during October 1991 to January 1992 and corresponds to the maximum of the optical depth (Figure 1a). The other four negative forcing maxima occur in spring and summer in the high latitudes of both hemispheres, with the two larger maxima in the Southern Hemisphere between 60°S and 70°S during December 1991 to February 1992 and during October 1992 to February 1993 and in the Northern Hemisphere between 55°N and 65°N during May–June 1992. These negative forcing maxima correlate with the midlatitude maxima of the optical depth and with the seasonal changes in solar irradiance and planetary albedo.

The longwave radiative forcings, $-\Delta R$, at TOA and the tropopause are presented in Figures 2e and 2f, respectively. These figures show that the longwave radiative forcing is positive at both levels and is about 3 W/m^2 larger at TOA than at the tropopause. This is the reason why the net radiative forcing at TOA is about 3 W/m^2 less negative than at the tropopause. The special feature of the longwave radiative forcing at TOA is the prolonged maximum located between 15°S and 15°N during September 1991 to April 1992, with a maximum value at 15°S in September 1991. The latter does not correspond to the maximum optical depth that occurs in December 1991 at about 2°S (Figure 1a) and probably is influenced by the change in effective temperature.

We can conclude that the difference between the instantaneous net radiative forcing at TOA and the tropopause is mostly due to the corresponding difference in the longwave forcing. As a result, the net radiative forcing at the tropopause is mostly due to the solar radiative forcing, and the net radiative forcing becomes less negative at the TOA than at the tropopause due to the increase in $-\Delta R$.

3. Parameterization of Volcanic Radiative Forcing Using a 1-D RTM

We have used our 1-D RTM to calculate the solar and longwave radiative forcing for the vertical distribution of aerosol optical depth given by *WMO* [1984] for volcanic conditions in an otherwise cloudless sky. The radiative forcing was calculated over a wide range of optical depths by varying the total aerosol optical depth while keeping fixed the relative contribution by each layer. The optical parameters of the aerosol were calculated for the spectral intervals of our RTM using the Mie-theory code which we used in the model intercomparison study of *Boucher et al.* [1998]. The aerosol had a lognormal size distribution with a mean radius of 0.2 μm and a chemical composition of 75% H_2SO_4 and 25% H_2O.

The solar radiative forcing by stratospheric aerosols, calculated by the 1-D RTM for the midlatitude summer atmospheric model of *McClatchey et al.* [1971], is presented in Figure 3 as a function of (1) optical depth averaged over 0.4 – 0.7 μm, $\bar{\tau}$, for solar zenith angles ζ = 40°, 60° and 80°, and albedos α = 0.2 (Figure 3a) and 0.4 (Figure 3b); (2) cosine of ζ for $\bar{\tau} = 0.0815$ and α = 0.2 and 0.4 (Figure 3c); and (3) α for $\bar{\tau} = 0.0815$ and ζ = 60°, (Figure 3d). These results show that the solar forcing linearly depends on optical depth to within ±10% and quadratically depends on both $\cos\zeta$ and α. A fit of these results applied to an arbitrary latitude ϕ and time t yields

$$\Delta S^{(1-D)}(\phi,t)=\left(\frac{\bar{\tau}(\phi,t)}{0.0815}\right)\times f_d(\phi,t)\times\left(-4.9453-11.147\cos\zeta(\phi,t)+16.604\cos^2\zeta(\phi,t)\right)\times\left(1.3575-0.3900\left(\frac{\alpha(\phi,t)}{0.2}\right)+0.0283\left(\frac{\alpha(\phi,t)}{0.2}\right)^2\right) \quad (1)$$

where we have included the weighting by the daylight fraction of a day, $f_d(\phi,t)$. Experiments with the 1-D RTM showed that without the daylight fraction included, the correlation of the shortwave forcing with the solar zenith angle is much less than with the daylight fraction included, especially where the cosine of the solar zenith angle is close to zero.

The longwave radiative forcing by stratospheric aerosols was calculated by the 1-D RTM for the midlatitude summer, tropical, and subarctic winter profiles of *McClatchey et al.* [1971]. The longwave radiative forcing is presented in Figure 4 as a function of the total optical depth $\bar{\tau}$ (Figure 4a) and ground temperature T (Figure 4b). To estimate the temperature influence on the values of longwave radiative forcing, a series of calculations was performed with fixed optical depth ($\bar{\tau} = 0.0808$) for different combinations of atmospheric temperature and humidity. A set of 11 atmospheric models was created using linear interpolation between the tropical and the subarctic winter temperature profiles at all altitudes. Two sets of calculations were carried out to estimate the influence of humidity on the calculated radiative forcing, one with the tropical humidity profile and the second with the subarctic winter humidity profile. The results show that the longwave radiative forcing linearly depends on optical depth and quadratically depends on temperature. As can be expected, the radiative forcing for fixed temperature is larger for low tropospheric humidity, but generally the influence of humidity is relatively small. A fit of these results applied to an arbitrary latitude ϕ and time t yields

$$\Delta R^{(1-D)}=-\left(\frac{\bar{\tau}}{0.0808}\right)\times\left(3.72-0.03933T(\phi,t)+1.0322\times10^{-4}T^2(\phi,t)\right) \quad (2)$$

The parameterizations given by equations (1) and (2) have an accuracy of about 5-10%. Applying them for annual, global-mean conditions ($f_d = 0.5, \cos\zeta = 0.479; \alpha = 0.245; T = 286$K) yields $\Delta N = -25.4\bar{\tau}$ W/m^2. This dependence of the net radiative forcing at TOA on optical depth is larger than the upper value of the estimates shown in Table 1 from *Stowe et al.* [1992], $\Delta N = -19.2\bar{\tau}$ W/m^2, where $\bar{\tau}$ is the optical depth at 0.55 μm wavelength.

Equations (1) and (2) cannot be used directly to represent the Pinatubo radiative forcing for three reasons: (1) the parameterizations apply only to clear-sky conditions, while the Pinatubo radiative forcing is the result of both clear-sky and cloudy conditions; (2) the results upon which equations (1) and (2) are based were obtained by changing only one factor at a time, while for the Pinatubo radiative forcing all factors could vary simultaneously; and (3) equations (1) and (2) apply to a single atmospheric column, while the Pinatubo radiative forcing in Figure 2 is the zonal mean around a latitude circle, and this zonal averaging can alter the dependencies in equations (1) and (2). Accordingly, below, we obtain parameterizations for the solar and longwave radiative forcing directly from the data of Figure 2 but informed by the dependencies shown by equations (1) and (2).

4. Fitting Radiative Forcing Calculated by 3-D RTM

In this section we obtain fits for the zonal-mean solar and longwave radiative forcing at TOA (1 hPa) and at the tropopause calculated by our 3-D RTM (Figure 2). Because the optical properties of the aerosol poleward of 75° latitude and prior to September 1991 were obtained by extrapolation in ST98, we do not use results for these spatial and temporal regions to obtain the

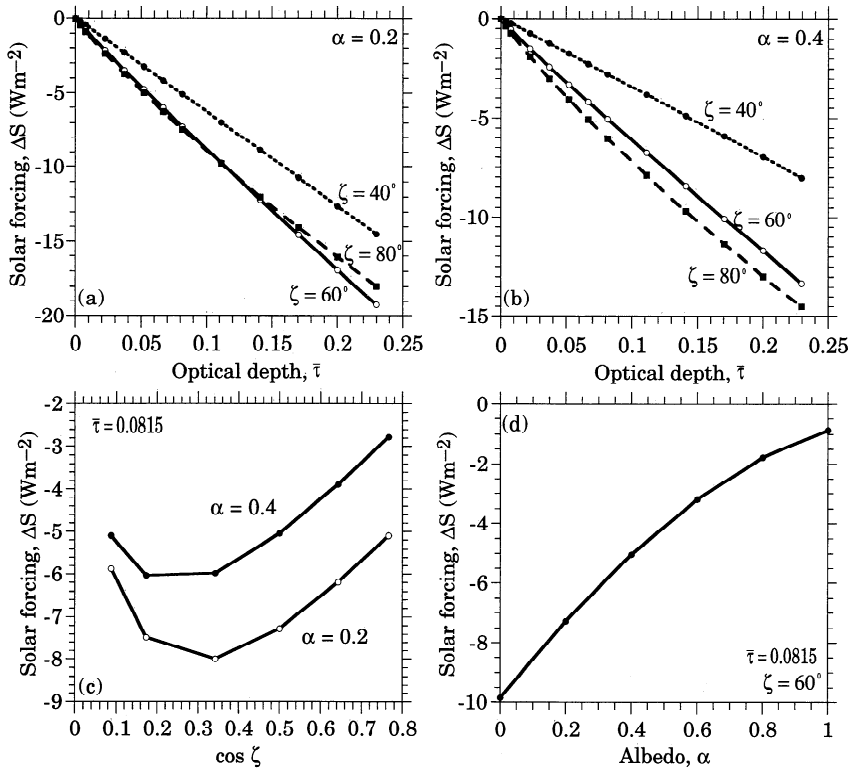

Figure 3. Solar radiative forcing ΔS calculated by the 1-D RTM as a function of (a, b) optical depth, τ, for solar zenith angles $\zeta = 40°$(dotted line), 60° (solid line), and 80° (dashed line) and albedos (a) $\alpha_s = 0.2$ and (b) $\alpha_s = 0.4$; (c) the cosine of the solar zenith angle for $\tau = 0.0815$; and (d) surface albedo for $\tau = 0.0815$ and solar zenith angle $\zeta = 60°$.

fits. However, we will use the complete data set to check the fits obtained. To estimate the goodness of the fits, we use the usual linear regression [*Wilks,* 1995] and the error expressed as the difference between the fit and the original data.

As we learned from the calculations by the 1-D RTM (section 3), the solar radiative forcing depends on the optical depth, the cosine of the solar zenith angle $\cos\zeta$, the daylight fraction of a day f_d, and the albedo. For the optical depth we will use the single-wavelength value at $\lambda = 0.55$ μm, $\tau_{0.55}$. This is the quantity that is available for the volcanoes antecedent to Pinatubo from SA93. For the albedo we will use the planetary albedo α_p, which will allow us to take into account the effects of clouds on the solar forcing. We will seek a fit for the solar forcing in the form suggested by equation (1):

$$\Delta S = g_1(\tau_{0.55} f_d) g_2(\cos\zeta) g_3(\alpha_p) \tag{3}$$

The longwave forcing in equation (2) depends on the optical depth and temperature. To take into account the effect of clouds on the longwave forcing, we will use the effective emitting temperature T_{eff}. We will seek a fit for the longwave forcing in the form suggested by equation (2):

$$\Delta R = f_1(\tau_{0.55}) f_2(T_{eff}) \tag{4}$$

To develop the fits, we therefore need the latitude-time distributions of (1) the zonal-mean $\cos\zeta$ calculated by the RTM (Figure 5a); (2) the daylight fraction of a day (Figure 5b); (3) the zonal-mean planetary albedo in the absence of the volcanic aerosol α_p simulated by the ST/GCM (Figure 5c); and (4) the zonal-mean effective emitting temperature $T_{eff} = (R/\sigma)^{1/4}$, where R is the outgoing longwave radiation at TOA simulated by the ST/GCM (Figure 5d), and σ is the Stefan-Boltzmann constant. Both R and α_p were taken from the corresponding control climate simulation mentioned in section 2.3.

4.1. Instantaneous Solar Radiative Forcing

4.1.1. Dependence on optical depth. To obtain the fit for the solar radiative forcing with respect to optical depth at 0.55 μm wavelength, we pooled all the data with the prescribed limitations (Figure 6a) and used linear regression with the constraint that the fit be zero for zero optical depth to obtain

$$\Delta S^{(1)} = -33.5\tau_{0.55}, \quad \rho = 0.88387 \tag{5}$$

where ρ is the correlation coefficient. The error of this fit, $\Delta S - \Delta S^{(1)}$, ranges from −3.56 to +4.73 W/m^2, with the largest values located in the high latitudes where seasonality plays a considerable role. The value $\Delta S^{(1)}/\tau_{0.55} = -33.5$ W/m^2 is close to estimate from *Stowe et al.* [1992] for the solar radiative forcing at TOA (Table 1).

4.1.2. Dependence on optical depth and planetary albedo. To include the planetary albedo in the fit of the solar radiative forcing along with optical depth, we introduce as a variable the product of the optical depth and the daylight fraction of a day. We defined the fit $\Delta S^{(1a)}$ of the dependence of ΔS on $(\tau_{0.55} f_d)$ by an automatic numerical procedure of drawing out a subpool of highly correlated data for the allowed small (within 1%) range of the values in other parameters, namely planetary albedo and $\cos\zeta$ (see Appendix for details):

$$\Delta S^{(1a)} = -49.739(\tau_{0.55} f_d), \quad \rho = 0.93525 \tag{6}$$

We defined the ratio $r_1 = \Delta S/\Delta S^{(1a)}$ and regressed the values of planetary albedo on r_1 to obtain

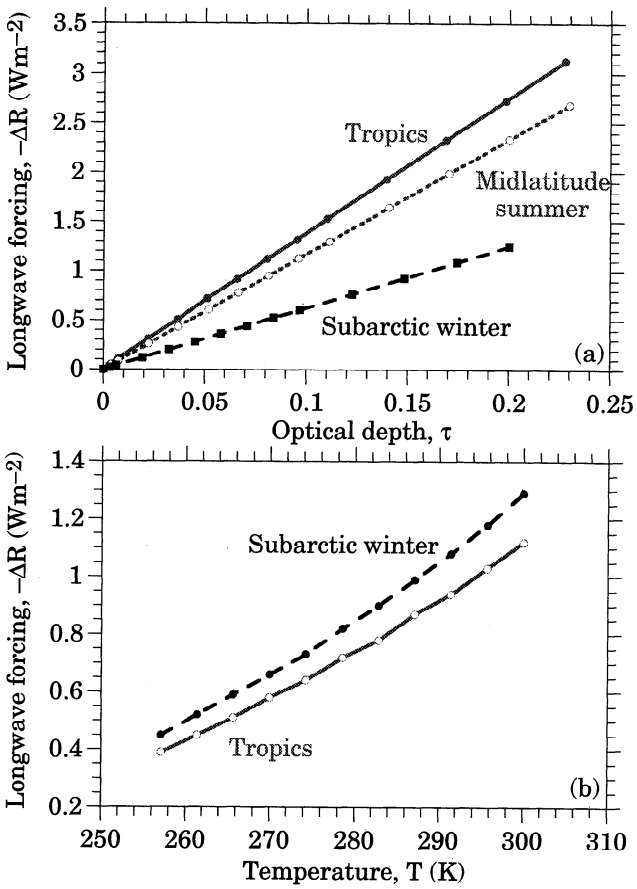

Figure 4. Longwave radiative forcing $-\Delta R$ calculated by the 1-D RTM as a function of (a) optical depthτ and (b) ground temperature for high (tropics) and low (subarctic winter) levels of tropospheric humidity.

$$\Delta S^{(2)} = -49.739\tau_{0.55} f_d \times (2.5706 - 5.9127\alpha_p + 4.3704\alpha_p^2), \quad \rho = 0.99128 \tag{7}$$

Fit $\Delta S^{(2)}$ has a much higher correlation with the original data than fit $\Delta S^{(1)}$. The difference $\Delta S - \Delta S^{(2)}$ ranges from –0.97 to +1.25 W/m^2, and the region of largest errors in the latitude–time domain is considerably reduced from that of $\Delta S - \Delta S^{(1)}$.

4.1.3. Dependence on optical depth, cosine of solar zenith angle, and planetary albedo. To include the dependence on cosζ in the fit, we regressed the cosine of the solar zenith angle data on $r_2 = \Delta S/\Delta S^{(2)}$ to obtain

$$\Delta S^{(3)} = -49.739\tau_{0.55} f_d \times (2.5706 - 5.9127\alpha_p + 4.3704\alpha_p^2) \times (1.1857 - 0.54196\cos\zeta - 0.42746\cos^2\zeta), \quad \rho = 0.99515 \tag{8}$$

The difference $\Delta S - \Delta S^{(3)}$ ranges from –0.85 to +0.91 W/m^2. Comparing the correlation coefficients for $\Delta S^{(2)}$ and $\Delta S^{(3)}$ shows that the latter is just a little larger than the former, but $\Delta S^{(3)}$ reproduces the geographical distribution of the solar radiative forcing considerably better than $\Delta S^{(2)}$.

4.1.4. Comparison with the fit obtained from the 1-D calculations. We used the fit obtained by the 1-D RTM, $\Delta S^{(1-D)}$ given by equation (1) for comparison with the errors $\Delta S - \Delta S^{(3)}$ and $\Delta S - \Delta S^{(1-D)}$. The values of $\Delta S - \Delta S^{(1-D)}$ range from –0.41 to +2.5 W/m^2, which is larger than the values of $\Delta S - \Delta S^{(3)}$. As expected, the correlation coefficient for $\Delta S^{(1-D)}$, $\rho = 0.98812$, is also lower than for $\Delta S^{(3)}$. Figure 7a shows the shortwave radiative forcing calculated using $\Delta S^{(1-D)}$ and $\Delta S^{(3)}$ plotted against the shortwave forcing calculated by the 3-D RTM. Every point in Figure 7a represents a specific latitude and a specific month. The fit built with the 3-D RTM data gives the location of the points closer to the "perfect line" than the fit obtained using the 1-D RTM, therefore the 3-D RTM fit gives a better result for more latitudes.

4.2. Instantaneous Longwave Radiative Forcing

4.2.1. Dependence on optical depth. As for the solar radiative forcing, we pooled the longwave radiative forcing data (Figure 6b) and used linear regression with the constraint that the fit be zero for zero optical depth to obtain

$$\Delta R^{(1)} = -11.945\tau_{0.55}, \quad \rho = 0.83483 \tag{9}$$

The difference $\Delta R - \Delta R^{(1)}$ ranges from –2.04 to +0.61 W/m^2 and most of the errors are located in high latitudes, which indicates that the longwave radiative forcing depends on the season. In addition, equation (9) does not reproduce the difference in time between the maximum $-\Delta R$, which occurs about 2 months earlier than the maximum optical depth.

4.2.2. Dependence on optical depth and effective temperature. To include the effective temperature T_{eff} in the fit of the longwave radiative forcing together with optical depth, we follow a procedure similar to that for fitting the shortwave radiative forcing. Specifically, we first define a fit $\Delta R^{(1a)}$ which represents the dependence of ΔR on the optical depth over a subpool of the data where ΔR and τ have their maximum correlation and where the change in T_{eff} is not more than 1% (see Appendix):

$$\Delta R^{(1a)} = -12.847\tau_{0.55}, \quad \rho = 0.87948 \tag{10}$$

Second, we regressed the effective temperature data on $\Delta R/\Delta R^{(1a)}$ to obtain

$$\Delta R^{(1a)} = -12.847\tau_{0.55} \times (23.134 - 0.20337 T_{eff} + 4.5096\times10^{-4} T_{eff}^2), \quad \rho = 0.99069 \tag{11}$$

The difference $\Delta R - \Delta R^{(2)}$ ranges from –0.37 to +0.62 W/m^2. Although $\Delta R^{(2)}$ underestimates the maximum $-\Delta R$ located in the region 15°S – 15°N from September 1991 to April 1992 on average by 10%, it correctly reproduces its time evolution.

4.2.3. Comparison with the fit obtained from the 1-D calculations. We used the fit obtained by the 1-D RTM, $\Delta R^{(1-D)}$ given by equation (2), to compare the errors $\Delta R - \Delta R^{(2)}$ and $\Delta R - \Delta R^{(1-D)}$. The values of $\Delta R - \Delta R^{(1-D)}$ range from –0.09 to +2.6 W/m^2, which is larger than the values for $\Delta R - \Delta R^{(2)}$. The correlation coefficient for $\Delta R^{(1-D)}$, $\rho = 0.98906$, is also lower than for $\Delta R^{(2)}$. It can be seen from Figure 7b that $\Delta R^{(1-D)}$ strongly underestimates the larger values of ΔR.

4.3. Representation of the instantaneous net radiative forcing

In subsequent calculations we will use $\Delta S^{(3)}$ and $\Delta R^{(2)}$ based on the 3-D RTM calculation rather than $\Delta S^{(1-D)}$ and $\Delta R^{(1-D)}$ based on the 1-D RTM calculation, because the former yields a better goodness of fit for all latitudes. The latitude-time distribution of the zonal-mean net radiative forcing at TOA (1 hPa) cal-

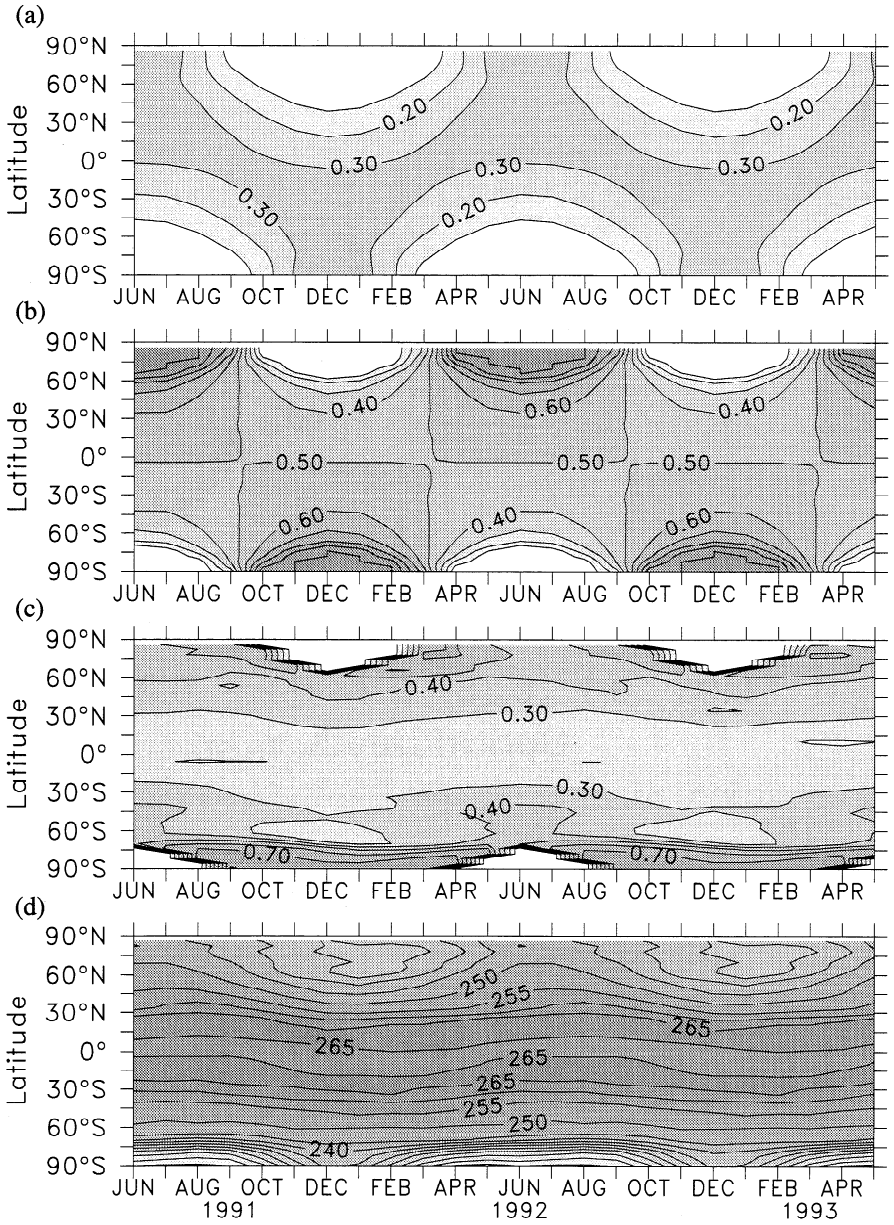

Figure 5. Time-latitude distributions of (a) solar zenith angle, (b) fraction of the daylight part of the day f_d, (c) planetary albedo in the absence of the volcanic aerosol α_p, and (d) effective emitting temperature T_{eff} from June 1991 to May 1993.

culated by the 3-D RTM and by $\Delta S^{(3)} - \Delta R^{(2)}$ are presented in Figure 8, together with their difference. The result shows reasonable agreement between the fit and the original data for the entire region 90°S – 90°N, July 1991 to May 1993, even though the fit was made only over the limited space-time domain 75°S – 75°N, September 1991 to May 1993. The fit reproduces the net radiative forcing with differences between –1.04 and 1.49 W/m^2, with the largest differences in the high latitudes where the smallest values of the net radiative forcing occur. The fit successfully captures the seasonal behavior of the zonal-mean net radiative forcing.

Figure 7c shows the net radiative forcing calculated using $\Delta S^{(3)} - \Delta R^{(2)}$ and a linear fit of all values of the net radiative forcing at TOA,

$$\Delta N^{(L)} = -21.58\tau_{0.55}, \quad \rho = 0.81103 \qquad (12)$$

plotted against the net forcing calculated by the 3-D RTM. It can be seen that using the more comprehensive fit $\Delta S^{(3)} - \Delta R^{(2)}$, yields a much more accurate estimation of the net radiative forcing at TOA than $\Delta N^{(L)}$. Also, from Figure 7c it can be seen that in general, the fit $\Delta S^{(3)} - \Delta R^{(2)}$ overestimates the negative values of the net radiative forcing. This occurs because in obtaining the fit we required the forcing to be equal to zero when the optical depth is zero, hence we did not include a constant term in equations (6) and (10). The estimate of the net radiative forcing at TOA by equation (12) is a little larger in magnitude than the previous estimates shown in Table 1.

The corresponding temporal variation of the hemispheric-mean and global-mean net radiative forcing at TOA calculated using both the $\Delta N^{(L)}$ and the $\Delta S^{(3)} - \Delta R^{(2)}$ parameterizations are given in Figure 9. It can be seen that for both hemispheres the $\Delta S^{(3)} - \Delta R^{(2)}$ fit is closer to the hemispheric-mean net radia-

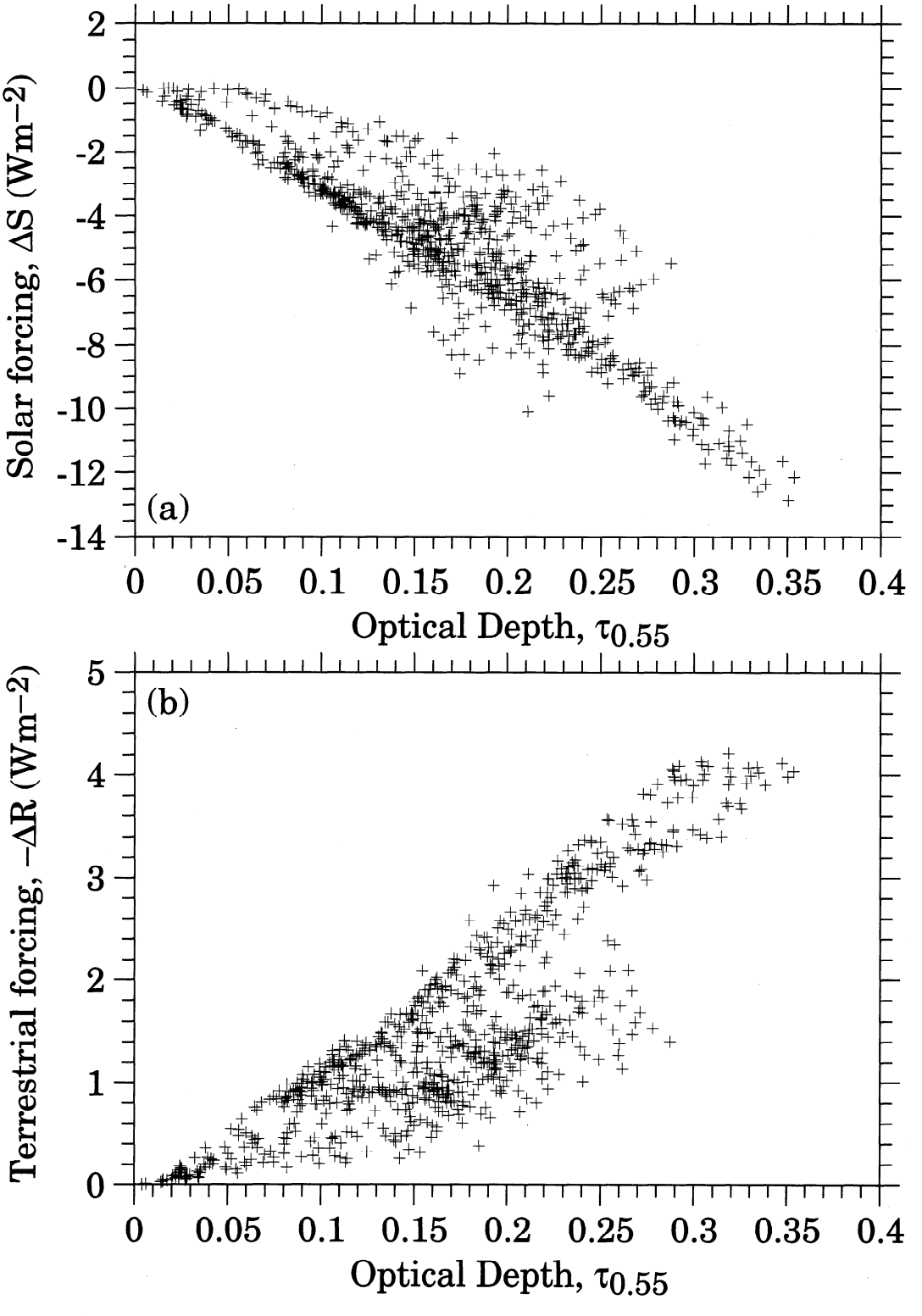

Figure 6. Dependence on the optical depth of (a) solar radiative forcing ΔS and (b) longwave radiative forcing $-\Delta R$ calculated by the 3-D RTM.

tive forcing calculated by the 3-D RTM than the linear fit $\Delta N^{(L)}$. However, for the global-mean net radiative forcing, both fits capture the shape and magnitude of the original data, with the $\Delta S^{(3)} - \Delta R^{(2)}$ fit being only slightly better than the $\Delta N^{(L)}$ fit. In general, one can use the linear fit $\Delta N^{(L)}$ for the global-mean net radiative forcing but not for the hemispheric means or for the geographical distribution of the net radiative forcing, where seasonally it plays an important role.

4.4. Further Evaluation of the Fit for radiative forcing

To further evaluate the fits of the solar and longwave radiative forcings that we have constructed using observations of the Pi-

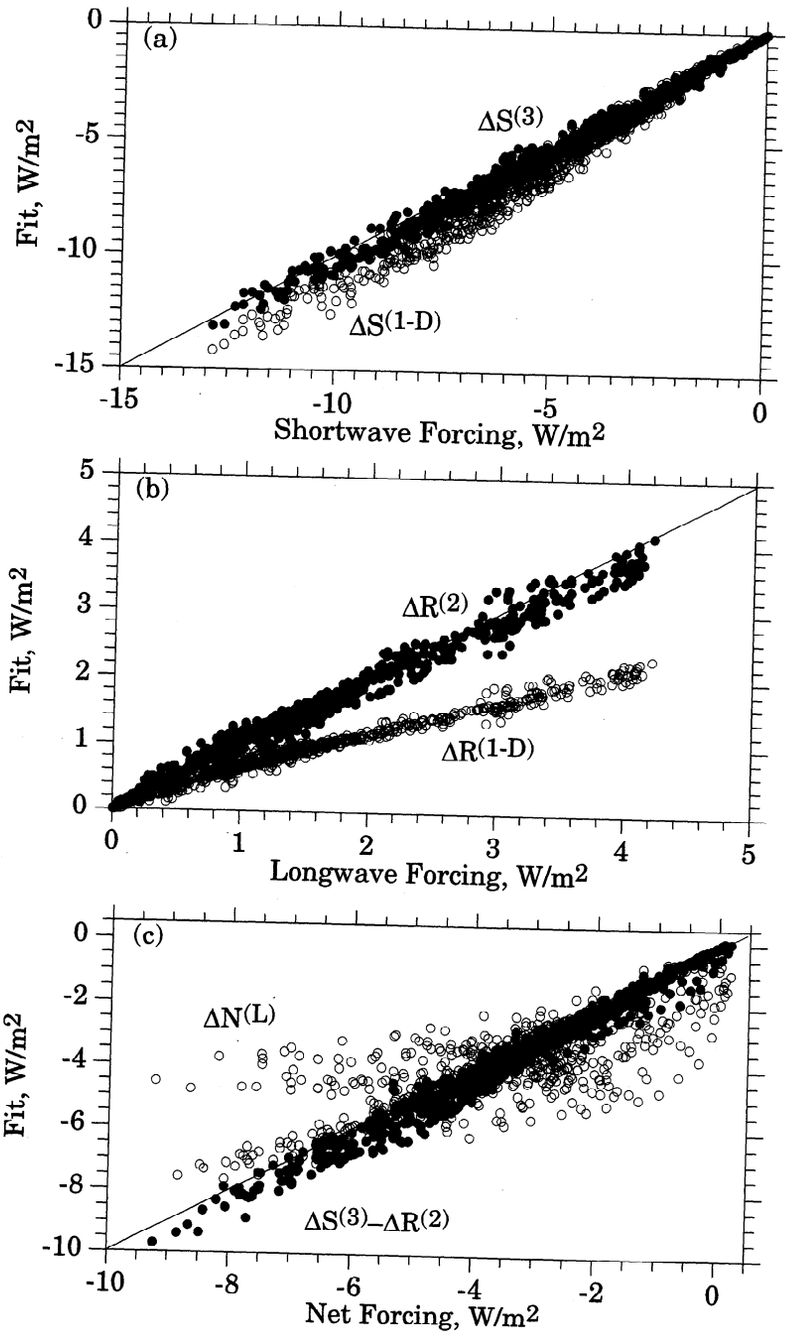

Figure 7. Correlation between (a) solar radiative forcing calculated by the 3-D RTM and the individual fits $\Delta S^{(3)}$ and $\Delta S^{(1-D)}$, (b) the longwave radiative forcing calculated by the 3-D RTM and the individual fits $\Delta R^{(2)}$ and $\Delta R^{(1-D)}$, and (c) the net radiative forcing calculated by 3-D RTM and the individual fits $(\Delta S^{(3)} - \Delta R^{(2)})$ and $\Delta N^{(L)}$.

natubo volcanic aerosols, it would be most useful to have corresponding observations for at least one volcano antecedent to Pinatubo. Regrettably, however, such observations do not exist. Accordingly, we further evaluate the fit by using four surrogate volcanic eruptions, which we have constructed by shifting the patterns of the specific extinction, single-scattering albedo, and asymmetry factor for the Pinatubo volcano (Figure 10): (1) northward by 24°, (2) northward by 60°, (3) southward by 60°, and (4) downward by five layers of the UIUC 24-layer troposphere/stratosphere GCM, such that the maximum eruption height decreased from about 10 hPa to the tropopause. We calculated the solar and longwave radiative forcings for each surrogate volcano by our 3-D RTM and compared them with the forcings calculated by $\Delta S^{(3)}$ and $\Delta R^{(2)}$ from the optical depths and the four other parameters saved from the 24-layer ST/GCM control simulation. To save computing time, we calculated the surrogate forcing for each hour of only the first day of each month instead of for all days of the month, as we did for the actual Pinatubo eruption (section 2.3). The error incurred by this computational economy is less than 3% in the tropics and 6% in high latitudes. For the surrogate forcing by $\Delta S^{(3)}$ and $\Delta R^{(2)}$ we used the solar insolation, effective emitting temperature, daylight fraction of a day, and planetary albedo as shown in Figure 5.

The values of the correlation coefficient over all latitudes between the radiative forcings by the 1-D fit $(\Delta S^{(1-D)} - \Delta R^{(1-D)})$ and the 3-D RTM and between the 3-D fit $(\Delta S^{(3)} - \Delta R^{(2)})$ and the

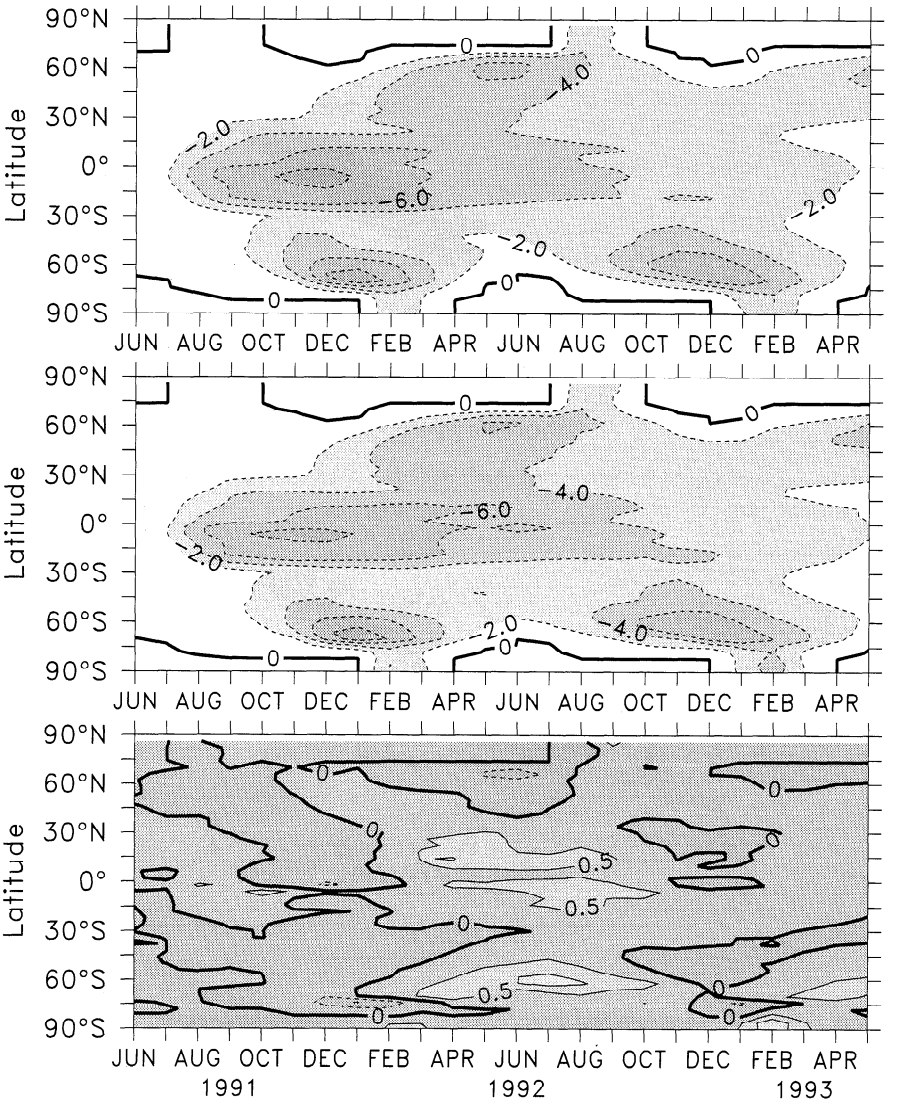

Figure 8. Latitude-time distributions of the zonal-mean net radiative forcing at TOA (1 hPa) calculated by the 3-D RTM (top), the fit $\Delta S^{(3)} - \Delta R^{(2)}$ (middle), and their difference (bottom).

3-D RTM, when the values for all months are pooled, are presented in Figure 11 in the form of box-plots. It is seen that in general, the 3-D fit works well for all the surrogate volcanic eruptions, although the interquartile distance for the surrogate eruptions (shown as 3-D with shift) is larger than for the Pinatubo eruption (shown as "No shift"), the correlation is not less than 0.9 for any case. The highest correlations belong to the tropical regions and the lowest correlations to the polar regions of both hemispheres. Figure 12 shows the hemispheric means for all surrogate volcanoes. It can be seen that the fit captures correctly the seasonal behavior of the original forcing, and the difference between the fit and the original forcing does not exceed 1 W/m^2 for any case.

4.5. Representation of adjusted tropopause net radiative forcing

As mentioned in section 1, to estimate the climatic effect of volcanic aerosols, one should use the "adjusted" radiative forcing at the tropopause, i.e., the radiative forcing after the stratospheric temperatures have adjusted radiatively to the perturbation. Here we present a simple way of doing this by using our calculations of the instantaneous radiative forcing. First, we present the parameterization of the instantaneous radiative forcing at the tropopause. Then we present the calculation of the adjusted forcing on the basis of this parameterization and experiments with the 1-D RTM which help to translate the instantaneous forcing at the tropopause into the adjusted forcing.

4.5.1. Parameterization of instantaneous net radiative forcing at tropopause. The instantaneous net radiative forcing calculated at the tropopause consists of the shortwave forcing ΔS, which is almost the same as the shortwave forcing at TOA (80% of the points have a difference less than 5%, and the largest differences occur for the smallest values of the forcing), and the longwave forcing $-\Delta R$, which is much smaller at the tropopause than at TOA (see Figure 2). Accordingly, we use $\Delta S^{(3)}$ for the shortwave radiative forcing at the tropopause, and

$$-\Delta R^{(TR)} = 4.226\tau; \quad \rho = 0.9717 \tag{13}$$

for the longwave radiative forcing at the tropopause. Equation (13) gives absolute errors in the range (–0.3, 0.2) W/m^2, which is superior to the range of (–0.2, 0.5) W/m^2 obtained when we include in the parameterization for $-\Delta R^{(TR)}$ an effective emitting

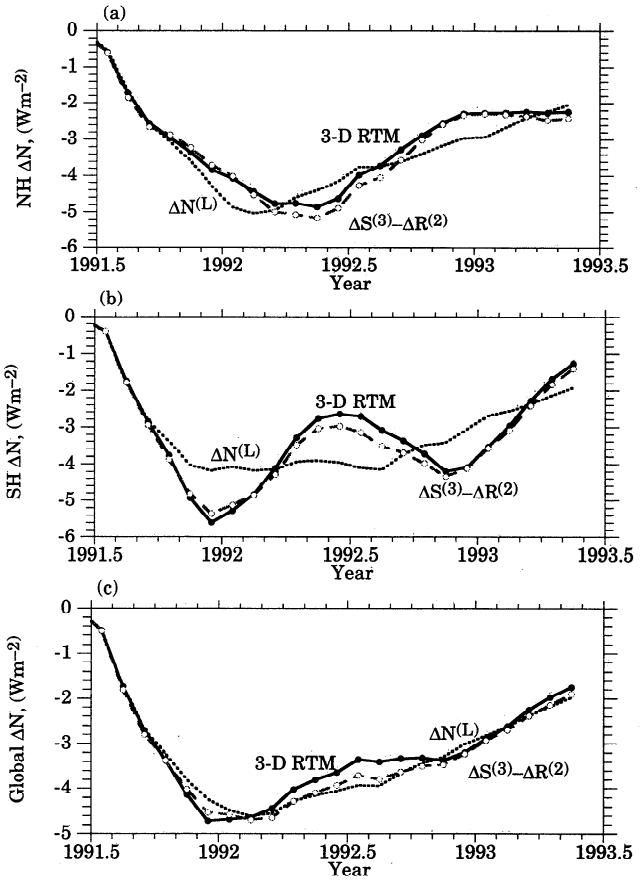

Figure 9. (a, b) Hemispheric-mean and (c) global-mean net TOA radiative forcing calculated by the 3-D RTM and by the fits $\Delta N^{(L)}$ and $\Delta S^{(3)} - \Delta R^{(2)}$.

temperature for the overlying atmosphere, similar to what we did for the parameterization for the longwave radiative forcing at TOA, $-\Delta R^{(2)}$. The parameterization for the instantaneous net radiative forcing at the tropopause, ($\Delta S^{(3)} - \Delta R^{(TR)}$), gives errors less than 10% for 90% of points located between 75°S and 75°N.

To compare the approximation ($\Delta S^{(3)} - \Delta R^{(TR)}$) with the parameterization given by *Hansen et al.* [1997] (Table 1), we linearly regressed the instantaneous net radiative forcing at the tropopause against the optical depth in the form $\beta\tau$ and obtained $\beta = -27.8$. The corresponding value for the data set obtained by the 3-D RTM is $\beta = -28.2$. These values are remarkably close to the value of $\beta = -28.4$ given by *Hansen et al.* [1997].

4.5.2. Calculation of adjusted net radiative forcing at tropopause. As defined above, the adjusted radiative forcing at the tropopause is the radiative forcing after the stratospheric temperatures have adjusted radiatively to the perturbation. The adjustment of the net radiative forcing occurs entirely in the longwave, and the value of the adjusted longwave radiative forcing $\Delta R^{(TR),adj}$ lies between the instantaneous longwave forcings at TOA, $\Delta R^{(2)}$, and at the tropopause, $\Delta R^{(TR)}$. Accordingly, we express $\Delta R^{(TR),adj}$ as

$$\Delta R^{(TR),adj} = \alpha \Delta R^{(TR)} + (1 - \alpha)\Delta R^{(2)} \quad (14)$$

with the interpolation factor α being in the range (0, 1). Equation (14) can be rewritten as

$$(\Delta R^{(TR),adj} - \Delta R^{(2)}) = \alpha\,(\Delta R^{(TR)} - \Delta R^{(2)}) \quad (15)$$

This allows us to estimate α from a regression of $(\Delta R^{(TR),adj} - \Delta R^{(2)})$ on $(\Delta R^{(TR)} - \Delta R^{(2)})$, using the instantaneous and adjusted longwave fluxes calculated by our 1-D RTM for different aerosol profiles in the stratosphere and different climatic conditions.

For the 1-D RTM calculation, selected atmospheric vertical profiles (pressure, temperature, water vapor, cloud water/ice, cloudiness, and ozone) and surface albedo, ground temperature, solar constant, and solar zenith angle were taken from the UIUC 24-layer ST/GCM control simulation (see section 2.3). To cover a wide range of climatic conditions and geographical locations, we chose profiles in January and July for latitudes between 74°S and 74°N, with an 8° interval, and longitudes between 0° and 360°, with 25° intervals. We tested two different vertical distributions of volcanic aerosol, one located in the atmospheric layer between 100 and 5 hPa, with a maximum loading of 70×10^{-9} g(SO_2)/g at 10 hPa; and another distribution located between 100 and 20 hPa, with a maximum loading of 10×10^{-9} g(SO_2)/g at 60 hPa. Altogether, we performed calculations for 366 different cases.

For each profile we first ran the 1-D RTM to equilibrium without volcanic aerosol. Then we added volcanic aerosol and ran the model to a new equilibrium with the ground and tropospheric temperatures fixed, and the stratospheric temperatures free to adjust radiatively. The resulting values of $(\Delta R^{(TR),adj} - \Delta R^{(2)})$ compared to $(\Delta R^{(TR)} - \Delta R^{(2)})$ give an estimate of α in equations (14) and (15) in the range 0.5 – 0.7, with a correlation of 0.93 for $\alpha = 0.6$. Accordingly, we have taken $\alpha = 0.6$ in these equations.

Finally, the net adjusted radiative forcing can be calculated as

$$\Delta N^{(TR),adj} = \Delta S^{(3)} - \Delta R^{(TR),adj} \quad (16)$$

Figure 13 shows the hemispheric and global means of the instantaneous net radiative forcing at the tropopause calculated by the 3-D RTM and approximated by $(\Delta S^{(3)} - \Delta R^{(TR)})$, together with the adjusted net radiative forcing approximated by $(\Delta R^{(TR),adj} - \Delta R^{(2)})$. As expected, the instantaneous radiative forcing at the tropopause is larger in magnitude than the instantaneous forcing at TOA (see Figure 9). From Figure 13 it can be seen that the adjusted radiative forcing at the tropopause is smaller in magnitude than the instantaneous radiative forcing but only by less than 0.5 W/m^2. Comparison of the geographical distributions of the adjusted and instantaneous radiative forcings at the tropopause shows that on average, their difference is 0.23 W/m^2, with maximum values up to 1.2 W/m^2 located between –20°S and 20°N. This means that the adjustment of the stratospheric temperatures reduces the net radiative forcing at the tropopause by not more than 15%.

We compared the values of the coefficient β at the tropopause obtained by regression of the net instantaneous and adjusted radiative forcings $\Delta N^{(TR)}$ and $\Delta N^{(TR),adj}$ against optical depth and obtained $\beta = -27.8$ and $\beta = -25.4$, respectively. These values are in agreement with those found by *Hansen et al.* [1997] (Table 1).

5. Net Radiative Forcing by Volcanoes From 1850 to 1994

We have used the fits obtained from the 3-D RTM, $S^{(3)} - R^{(2)}$, and $\Delta S^{(3)} - \Delta R^{(TR),adj}$ to reconstruct the instantaneous net TOA and adjusted tropopause radiative forcing by volcanoes from 1850 to 1994. To do this, we used the monthly latitudinal distributions of zonal-mean optical depths at 0.55 μm for

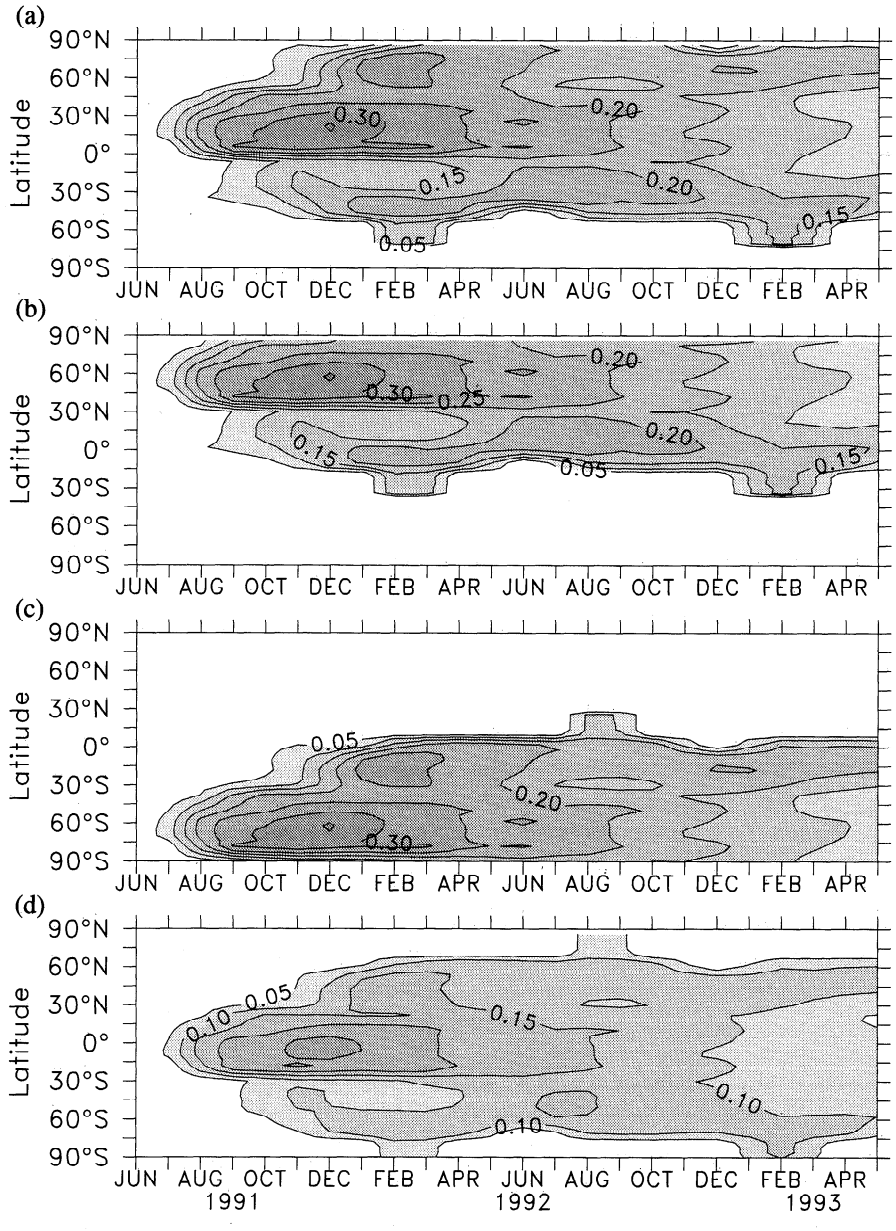

Figure 10. Latitude-time distributions of optical depth $\tau_{0.55}$ for four surrogate volcanic eruptions obtained by shifting the pattern of specific extinction, single-scattering albedo, and asymmetry factor for the Mount Pinatubo volcano: (a) northward by 24°, (b) northward by 60°, (c) southward by 60°, and (d) downward by five layers of the UIUC 24-L AGCM, such that the maximum eruption height decreased from 25 km to about the tropopause.

1850-1990 compiled by SA93, which are available and updated through 1994 at http://molscat.giss.nasa.gov/data/strataer/. The values of α_p, T_{eff}, and $\cos\zeta$ were taken from the control simulation by our 24-layer ST/GCM and shown in Figure 5. These data are available at http://crga.atmos.uiuc.edu.

As mentioned by SA93, the uncertainty in the estimated stratospheric aerosol optical depth tends to increase as we go farther back in time. SA93 subjectively estimated that typical errors in the estimation of the optical depth are about 50% for 1850–1915 and 25% for 1915-1990. Accordingly, the net radiative forcing estimated for 1850–1990 has similar uncertainties. For the Pinatubo eruption, however, an estimation of the radiative forcing can be made more accurately. In Figure 14 we compare the hemispheric optical depths of SA93 for the Pinatubo volcano with our calculated optical depths (section 2), as well as the corresponding net adjusted radiative forcings at the tropopause calculated by $\Delta N^{(TR),adj}$. As can be seen, our optical depths are larger than those of SA93, who compiled the aerosol optical depths for the Pinatubo period using the SAGE II data for $\lambda = 0.55$ μm (section 2). As a result, the radiative forcing calculated using the fit $\Delta N^{(TR),adj}$ with the SA93 optical depths is on average smaller than the radiative forcing calculated using the same fit with our optical depths. Accordingly, for the reconstruction of the volcano forcing from 1850 to 1994 we use the optical depths of SA93 until the beginning of the Pinatubo eruption, i.e., June 1991. Thereafter, we use our optical depths interpolated to the latitudinal grid of the SA93 data. As mentioned on the http://molscat.giss.nasa.gov/data/strataer/ website, the SA93 optical depths for the period of the El Chichón eruption were revised by the authors on the basis of the then-most-recent publications. Here we have done the same for the period of the Pinatubo eruption.

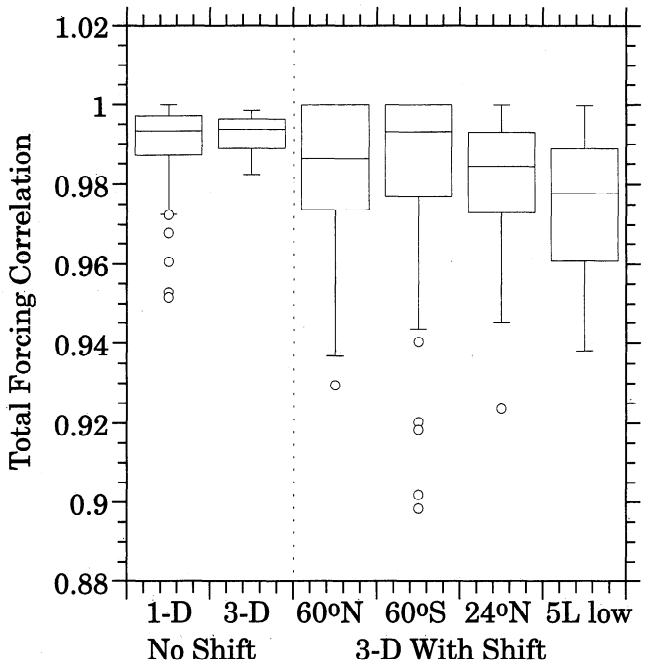

Figure 11. The box-plots for the correlation between the latitude-time distributions of net TOA radiative forcing calculated by the 3-D RTM and the fit $\Delta S^{(1-D)} - \Delta R^{(1-D)}$ for the Pinatubo volcano ("No shift") and between the 3-D RTM and the fit $\Delta S^{(3)} - \Delta R^{(3)}$ for four surrogate volcanoes (24°N, 60°N, 60°S, 5L low). Here the outlier data are shown by circles. Outliers are the points whose value is either $> UQ + 1.5 \times IQD$ or $< LQ - 1.5 \times IQD$, where UQ is the upper quartile (the data value located halfway between the median and the highest data value), LQ is the lower quartile (the data value located halfway between the median and the lowest data value), and IQD is interquartile distance, which is equal to $UQ - LQ$.

The resulting evolution of the zonal-mean adjusted net radiative forcing at the tropopause by volcanoes, based on our revision of the optical depth of SA93 and calculated using the fit $\Delta N^{(TR),adj}$, is presented in Plate 1. It can be seen that the intensity of the volcanic activities during the second half of the 19th century was greater than for the first half of the 20th century and was less than for the second half of the 20th century. Thus a corresponding climatic effect should be expected: the largest cooling effect would belong to the last 50 years, and the smallest effect would belong to the first 50 years of the 20th century. Indeed, the global temperature-anomaly record for 1850–1995 [*Nicholls et al.*, 1996] shows that there is some positive change in temperature during the first half of the 20th century and this may correlate with the reduction in volcanic activity. After 1950 the positive temperature anomaly starts to decrease, and this may correlate with the increase in volcanic activity for the second half of the 20th century. However, beginning in the 1970s, the positive temperature anomaly started to increase rapidly in spite of the expected large cooling effect from volcanic activity. Therefore to estimate the relative importance of volcanoes for climate change, it is necessary to take into account other factors that may have influenced the radiative forcing, for example, greenhouse gases, tropospheric aerosol, and solar variability.

Plate 1 shows that the radiative forcings by different volcanic eruptions are not similar. This is more clearly seen in Figure 15 which shows that the adjusted radiative forcing at the tropopause by the volcanoes during 1883–1887 (Figure 15a) had a latitudinally wide signature. In contrast, the eruption of El Chichón in the Northern Hemisphere in 1982 (Figure 15c) had a narrow area of maximum negative forcing for half a year, with small values during the second year. Also it can be seen that the eruption of Agung in 1963 in the Southern Hemisphere (Figure 15b) and El Chichón in 1982, both with comparable forcing smaller in magnitude than –8.0 W/m^2, did not extend into the opposite hemi-

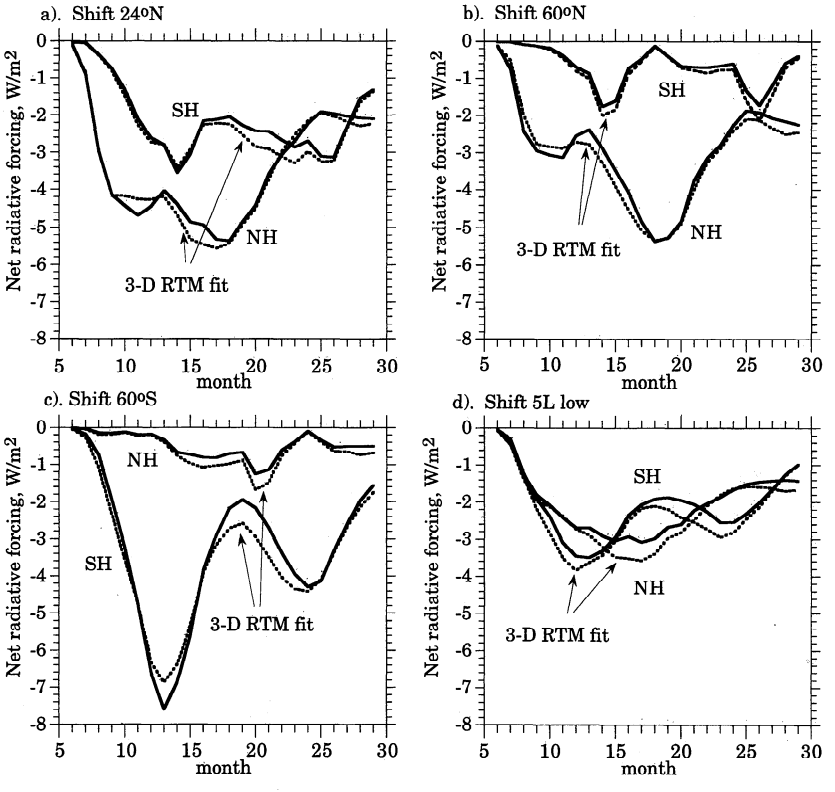

Figure 12. Net TOA radiative forcing calculated by the 3-D RTM and the fit $\Delta S^{(3)} - \Delta R^{(3)}$ for four surrogate volcanoes: (a) 24°N, (b) 60°N, (c) 60°S, (d) 5L low.

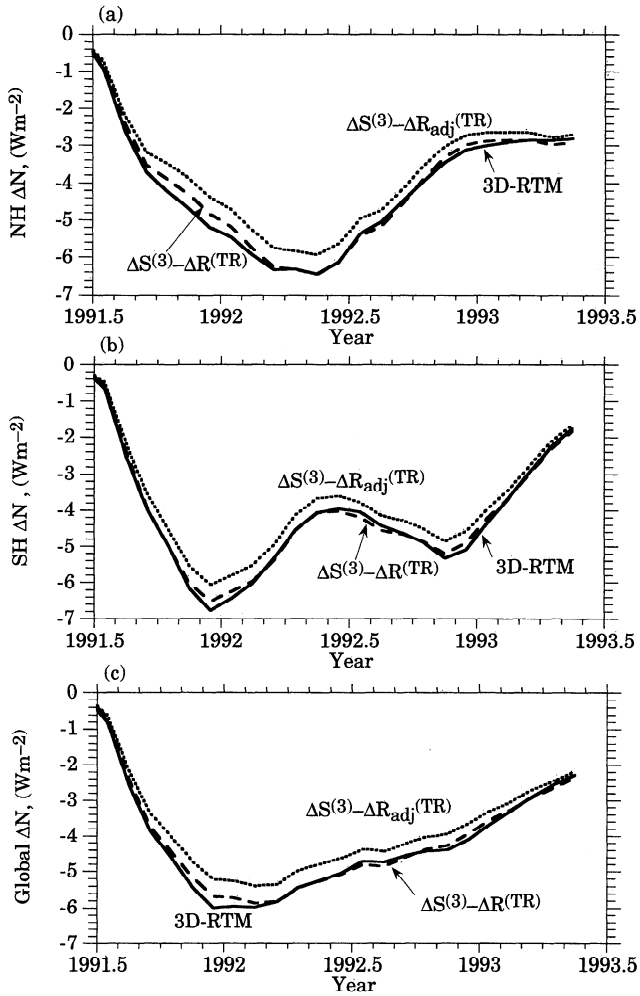

Figure 13. (a, b) Hemispheric-mean and (c) global-mean instantaneous net radiative forcing at the tropopause calculated by the 3-D RTM and by the fit ($\Delta S^{(3)} - \Delta R^{(TR)}$), and the adjusted net radiative forcing at the tropopause calculated by the fit $\Delta N^{(TR),adj}$.

sphere. The reasons for these differences in forcing are the geographical location of the volcanoes, the strength of the eruption, and the atmospheric circulation.

Figure 16 presents the hemispheric and global means of the adjusted net radiative forcing at the tropopause for the period from 1850 to 1994. Comparing Figures 16a and 16b shows that different volcanoes have different signatures for the two hemispheres. For example, Agung has a strong signature in the Southern Hemisphere but not in the Northern Hemisphere, El Chichón has a stronger signature in the Northern Hemisphere than in the Southern Hemisphere, while Krakatoa and Pinatubo have similar strong signatures in both hemispheres. From Figure 16c it can be seen that Krakatoa in mid-1885 yielded the largest global-mean net radiative forcing until the radiative forcing by Pinatubo in early 1992. The digital data of the calculated radiative forcing are available at http://crga.atmos.uiuc.edu.

6. Conclusion

In this paper we have developed parameterizations for the zonal-mean instantaneous and adjusted radiative forcing by volcanic aerosols in terms of their optical depth and the solar insolation, the planetary albedo in the absence of the volcanic aerosol, and the effective emitting temperature of the Earth. These parameterizations give reasonably good agreement with the radiative forcing calculated by the UIUC detailed radiative transfer model for the Pinatubo aerosol and for surrogate volcanoes having different latitudes and injection altitudes. We have applied these parameterizations to calculate the instantaneous and adjusted radiative forcings of volcanoes from 1850 to 1994. All data are available on the homepage at http://crga.atmos.uiuc.edu.

It should be noted that the volcanic radiative forcing calculated here has uncertainty as a result of (1) the uncertainty of the radiative forcing calculated by the 3-D RTM; (2) the uncertainty of the fit (parameterization) of the radiative forcing calculated by the RTM; and (3) the uncertainty of the input fields to the fit (parameterization) used to calculate the radiative forcing.

The uncertainty of the radiative forcing calculated by the 3-D RTM is difficult to quantify, mostly because there are no observations of the instantaneous radiative forcing (due only to the presence of the aerosol) with which to compare. However, it is likely that the uncertainty of the radiative forcing calculated here using the RTM of the UIUC ST/GCM is smaller than that of the ST98 calculation using the RTM of the ECHAM4 GCM because of the higher spectral and vertical resolution of the UIUC RTM.

We are able to estimate quantitatively the uncertainty of the parameterization of the radiative forcing calculated by the 3-D RTM. Using the data from Figure 9, it can be calculated that the uncertainty of the parameterization for the global instantaneous net radiative forcing at TOA, measured as a relative error is in the

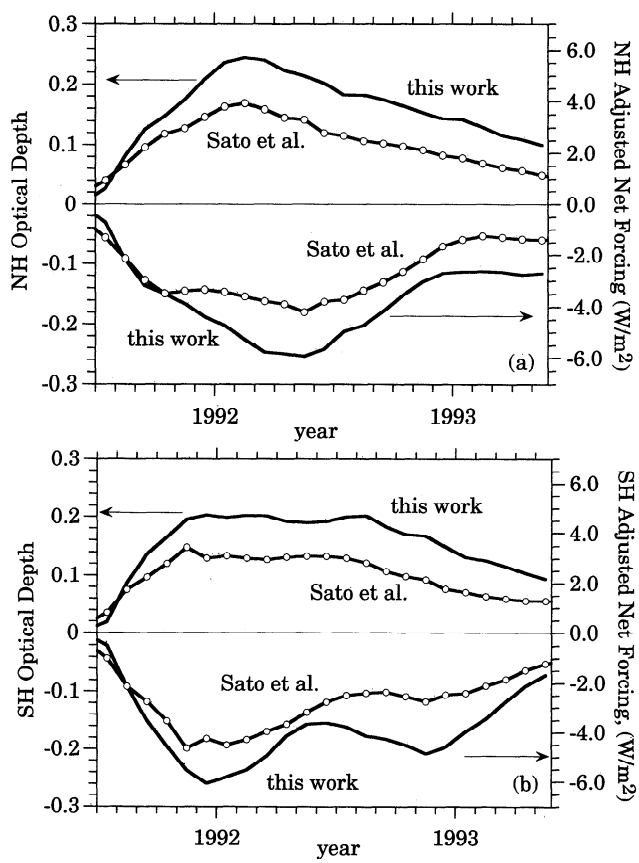

Figure 14. Comparison of the hemispheric means of the original optical depths from SA93 and the revised optical depths described in this paper for Pinatubo, presented together with correspondingly calculated the adjusted net radiative forcing at the tropopause: (a) Northern Hemisphere, (b) Southern Hemisphere.

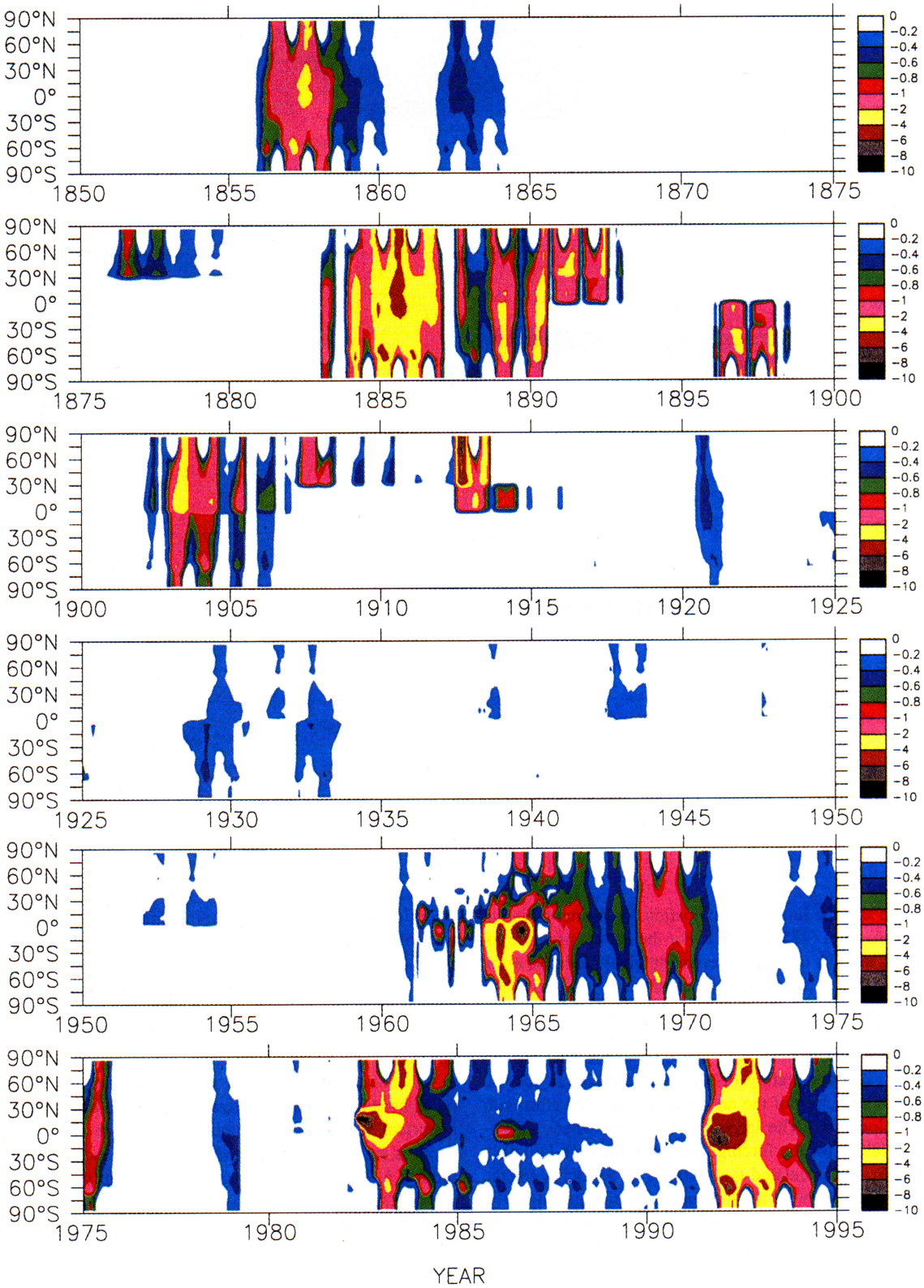

Plate 1. Zonal-mean adjusted net radiative forcing at the tropopause $\Delta N^{(TR),adj}$ from 1850 to 1994 calculated from the optical depths of SA93 for the periods January 1850 to June 1991 and June 1993 to December 1994 and from the optical depths calculated in this paper for Pinatubo period, July 1991 through May 1993.

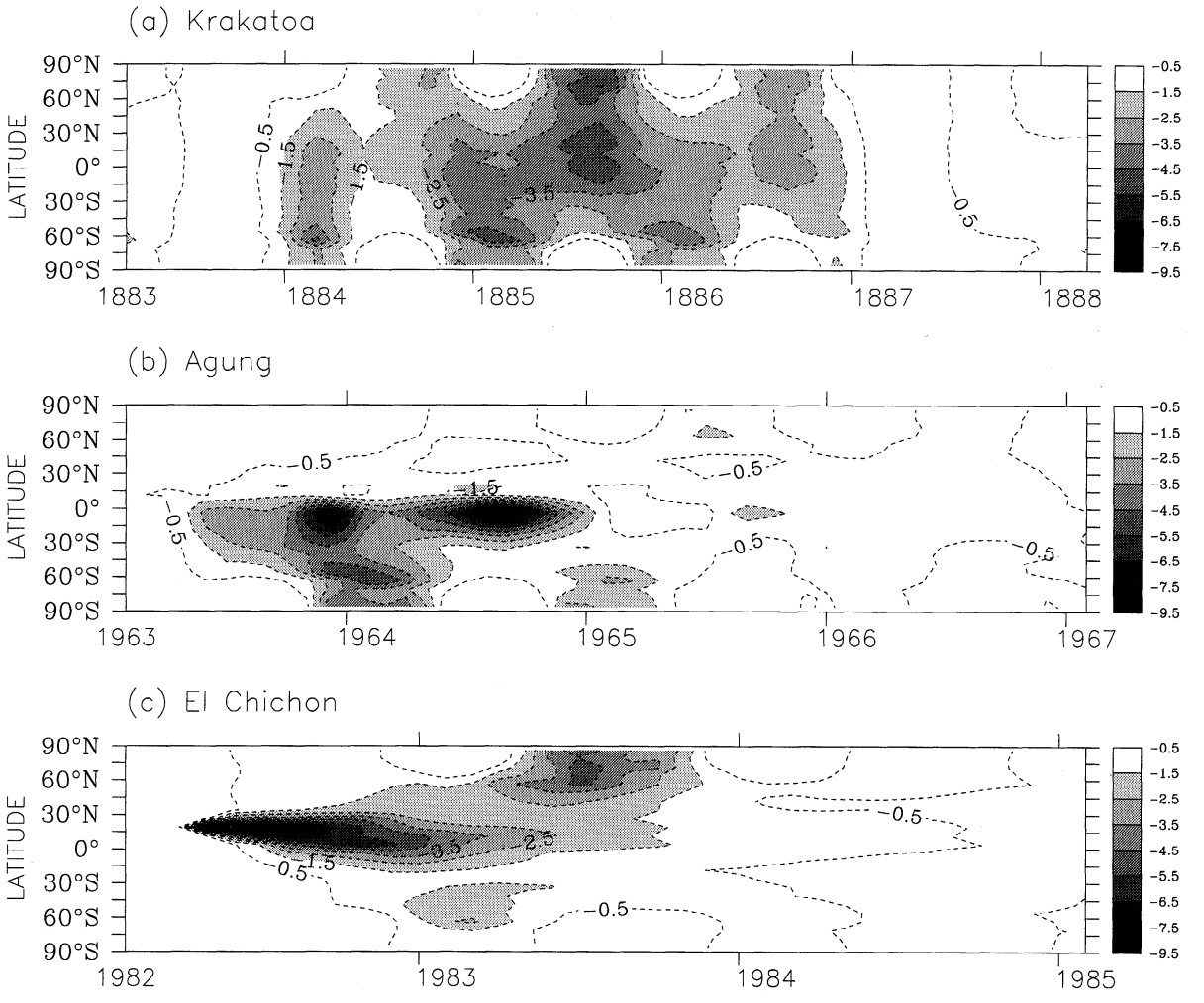

Figure 15. Zonal-mean adjusted net radiative forcing at the tropopause $\Delta N^{(TR),adj}$ calculated for (a) Krakatoa, (b) Agung, and (c) El Chichón from the optical depths of SA93.

range –15%, 5%. The linear approximation for the net radiative forcing at TOA gives (–25%, 10%). For the net hemispheric radiative forcing at TOA our parameterization gives a relative error of (–15%, 5%) for the Southern Hemisphere and (–10%, 5%) for the Northern Hemisphere. The linear approximation of the hemispheric radiative forcing gives a much larger error, (–55%, 25%) for the Southern Hemisphere and (–25%, 10%) for the Northern Hemisphere. The uncertainty of the parameterization for the geographical distribution of the net radiative forcing varies with geographical location. The largest errors occur where we obtained small values for the forcing, mostly in the high latitudes. From Figure 7c we calculated that within (75°S, 75°N), for the entire period of evolution of the Pinatubo aerosol from July 1991 to May 1993, only 4% of the 770 points have an error larger than 40%, and 60% of the points have an error less than 10%. For the linear approximation of the net radiative forcing at TOA the corresponding numbers are 23% for an error larger than 40% and 39% for an error less than 10%. The uncertainty of the parameterization of the instantaneous and adjusted radiative forcing at the tropopause have similar estimates. The error of any linear approximation $\beta\tau$ of the net forcing (instantaneous or adjusted, at TOA or at tropopause) obtained in this study are larger than the errors of the corresponding more-comprehensive parameterization obtained here. Therefore we conclude that the linear parameterization of the radiative forcing as a function of optical depth alone is applicable only for the global net radiative forcing, while our more comprehensive parameterization should be applied to calculate the hemispheric and zonal means of the net radiative forcing.

We believe that the only relevant uncertainty of the input fields used by the parameterization is for the optical depth of the historical volcanoes. The uncertainty in the estimated optical depth is smallest for the Pinatubo eruption and, as mentioned in section 5, increases with increasing time in the past. Here we have presented an improved estimation of the optical depths for the Pinatubo aerosol.

The overall uncertainty of the estimation of the radiative forcing from past volcanoes is large. Still, large uncertainties exist for the Pinatubo period. However, we believe that our work reduces the existing uncertainties in the calculation of the radiative forcing by volcanoes and that the parameterization developed here for the adjusted net, shortwave, and longwave forcing is useful for the calculation of the climatic effect of historical volcanoes.

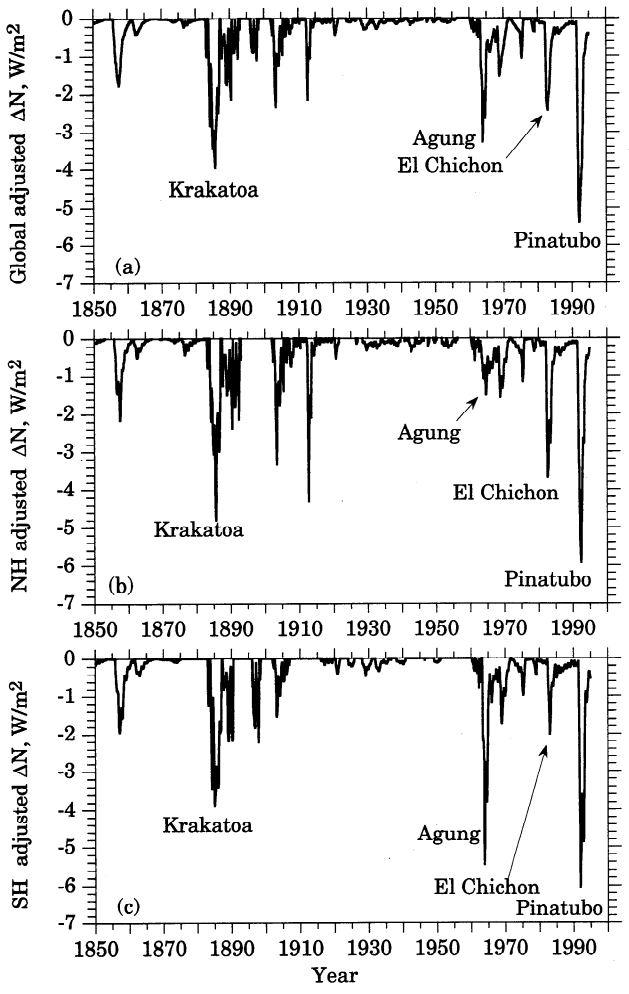

Figure 16. (a) Global-mean, (b) Northern Hemisphere, and (c) Southern Hemisphere adjusted net radiative forcing at the tropopause calculated by $\Delta N^{(TR),adj}$ from the optical depths of SA93 for the periods January 1850 to June 1991 and June 1993 to December 1994 and from the optical depths calculated in this paper for the Pinatubo period, July 1991 through May 1993.

Appendix: Automatic Numerical Procedure of Drawing Out Subpool of Highly Correlated Data

We wish to express $y = y(x_1, x_2, x_3)$ in the form $y = g_1(x_1)g_2(x_2)g_3(x_3)$ using the set of values $\{x_{1,i}, x_{2,i}, x_{3,i}, y_i; i = 1, \cdots, n\}$ obtained by binning the data for all months and latitudes. The functions g_1, g_2, and g_3 are determined in three steps.

First, subsets of size m are constructed according to the following "rules":

$$(1-q)x_{1,s} < x_{1,j} < (1+q)x_{1,s},$$
$$s = 1, \cdots, n-1; j = 1, \cdots, n-1, j \neq s; q \leq 0.05; \quad \text{(A1)}$$

$$(1-q)x_{2,s} < x_{2,j} < (1+q)x_{2,s},$$
$$s = 1, \cdots, n-1; j = 1, \cdots, n-1, j \neq s; q \leq 0.05; \quad \text{(A2)}$$

$$m > M > 10 \quad \text{(A3)}$$

The first two conditions constrain the values of x_1 and x_2 to be quasi-constant, and the third condition maximizes the size of the subsets. We maximize M and minimize q consistent with condition (A3). The best values for M and q are interactively determined for the subset that has the highest correlation between y and x_3. Finally, $g_3(x_3)$ is obtained using a polynomial fitting.

Second, the dependence of y/g_3 on x_2 is determined. Subsets of size m are constructed according to the following "rules":

$$(1-q)x_{1,s} < x_{1,j} < (1+q)x_{1,s},$$
$$s = 1, \cdots, n-1; j = 1, \cdots, n-1, j \neq s; q \leq 0.05; \quad \text{(A1)}$$

$$m > M > 10 \quad \text{(A2)}$$

Then $g_2(x_2)$ is determined a polynomial fitting for the subset with the highest correlation between $y/g_3(x_3)$ and x_2.

Third and lastly, $g_1(x_1)$ is determined using a polynomial fitting for $y/[g_3(x_3)g_2(x_2)]$ on x_1 using all the data.

Acknowledgments. This study was supported by the National Science Foundation and the Carbon Dioxide Research Program, Office of Health and Environmental Research of the Department of Energy under grant ATM-9522681, and by NASA under grant NAG53739 and NSF under grant ATM-9528201.

References

Boucher, O., and U. Lohmann, The sulfate-CCN-cloud albedo effect, *Tellus, Ser. B., 47,* 281-300, 1995.

Boucher, O., et al., Intercomparison of models representing direct shortwave radiative forcing by sulfate aerosols, *J. Geophys. Res., 103,* 16,979-16,998, 1998.

Chou, M. D., Parameterizations for the absorption of solar radiation by O_2 and CO_2 with application to climate studies, *J. Clim., 3,* 209-217, 1990.

Chou, M. D., A solar radiation model for use in climate studies, *J. Atmos. Sci., 49,* 762-772, 1992.

Chou, M. D., and K. T. Lee, Parameterizations for the absorption of solar radiation by water vapor and ozone, *J. Atmos. Sci., 53,* 1203-1208, 1996.

Chou, M. D., and M. J. Suarez, An efficient thermal infrared radiation parameterization for use in General Circulation Models, NASA Technical Memorandum 104606, Vol. 3, 85 pp., 1994.

Chou, M., L. Peng, and A. Arking, Climate studies with a multilayer energy balance model, III, Climatic impact of stratospheric volcanic aerosols, *J. Atmos. Sci., 41,* 759-767, 1984.

Hansen, J., R. Ruedy, A. Lacis, G. Russell, M. Sato, J. Lerner, and D. Rind, Wonderland climate model, *J. Geophys. Res., 102,* 6823-6830, 1997.

Harshvardhan, Perturbation of the zonal radiation balance by a stratospheric aerosol layer, *J. Atmos. Sci., 36,* 1274-1285, 1979.

Harvey, L. D. D., J. Gregory, M. Hoffert, A. Jain, M. Lal, R. Leemans, S. B. C. Raper, T. M. L. Wigley, and J. de Wolde, An Introduction to Simple Climate Models, in IPCC Second Assessment Report, 50 pp., Intergov. Panel on Clim. Change, Bracknell, England, 1997.

King, M. D., and Harshvardhan, Comparative accuracy of selected multiple scattering approximations, *J. Atmos. Sci., 43,* 784-801, 1986.

Lacis, A., J. Hansen, and M. Sato, Climate forcing by stratospheric aerosols, *Geophys. Res. Lett., 19,* 1607-1610, 1992.

Langner, J., and H. Rodhe, A global three dimensional model of the tropospheric sulfur cycle, *J. Atmos. Chem., 13,* 225-263, 1991.

Long, C. S., and L. L. Stowe, Using the NOAA/AVHRR to study stratospheric aerosol optical thickness following the Mt. Pinatubo eruption, *Geophys. Res. Lett., 21,* 2215-2218, 1994.

McClatchey, R. A., R. W. Fenn, J. E. A. Selby, F. E. Volz, and J. S. Garing, *Optical Properties of the Atmosphere,* AFCRL-71-0279, 85 pp.,Air Force Cambridge Res. Lab., Bedford, Mass., 1971.

Minnis, P., E. F. Harrison, L. L. Stowe, G. G. Gibson, F. M. Denn, D. R. Doelling, and W. L. J. Smith, Radiative climate forcing by the Mount Pinatubo eruption, *Science, 259,* 1411-1415, 1993.

Nicholls, N., G. V. Gruza, J. Jouzel, T. R. Karl, L. A. Ogallo, and D. E. Parker, Observed climate variability and change, in *Climate Change 1995: The Science of Climate Change,* edited by J. T. Houghton, L. G. Meira Filho, B. A. Callander, N. Harris, A. Kattenberg, and K. Maskell, pp. 133-192, Cambridge Univ. Press, New York, 1996.

Pollack, J. B., O. B. Toon, C. Sagan, A. Summers, B. Baldwun, and W. VanCamp, Volcanic explosions and climatic change: A theoretical assessment, *J. Geophys. Res., 81,* 1071-1083, 1976.

Sato, M., J. E. Hansen, M. P. McCormick, and J. B. Pollack, Stratospheric aerosol optical depths, 1850-1990, *J. Geophys. Res., 98,* 22,987-22,994, 1993.

Schimel, D., et al., Radiative forcing of climate change, in *Climate Change 1995: The Science of Climate Change,* edited by J.T. Houghton, L. G. Meira Filho, B. A. Callander, N. Harris, A. Kattenberg, and K. Maskell, pp. 65-132, Cambridge Univ. Press, New York, 1996.

Slingo, A., A GCM parameterization for the shortwave radiative properties of water clouds, *J. Atmos. Sci., 46,* 1419-1427, 1989.

Stenchikov, G. L., I. Kirchner, A. Robock, H.-F. Graf, J. C. Antuña, R. G. Grainger, A. Lambert, and L. Thomason, Radiative forcing from the 1991 Mt. Pinatubo volcanic eruption, *J. Geophys. Res., 103,* 13,837-13,857, 1998.

Stowe, L. L., R. M. Carey, and P. P. Pellegrino, Monitoring the Mt. Pinatubo Aerosol Layer with NOAA/11 AVHRR Data, *Geophys. Res. Lett., 19*(2), 159-162, 1992.

Wilks, D. S., *Statistical Methods in the Atmospheric Sciences,* 465 pp., Academic, San Diego, Calif., 1995.

World Meteorological Organization (WMO), *Report of the expert meeting on aerosols and their climatic effects,* 107 pp., World Clim. Res. Program, Geneva, 1984.

N. G. Andronova, E. V. Rozanov, M. E. Schlesinger, and F. Yang, Department of Atmospheric Sciences, University of Illinois at Urbana-Champaign, 105 S. Gregory Street, Urbana, IL 61801. (natasha@uiatma.atmos.uiuc.edu)

G. L. Stenchikov, Department of Environmental Sciences, Rutgers University, 14 College Farm Rd., New Brunswick, NJ 08901-8551.

(Recieved October 2, 1998; revised January 19, 1999;
accepted February 23, 1999.)